JGR Oceans

RESEARCH ARTICLE
10.1029/2019JC015086

Interannual Variability of Mixed Layer Dynamics in the Ecuadorian Ocean

Maria J. Marin Jarrin[1] and Thomas C. Lippmann[2]

[1]Department of Earth Sciences, University of Oregon, Eugene, OR, USA, [2]Department of Earth Sciences, Center for Coastal and Ocean Mapping, University of New Hampshire, Durham, NH, USA

Key Points:
- Observed ocean temperature structure obtained over 22 years in the coastal Ecuadorian Sea is coupled with variations west of the Galapagos
- Interannual ENSO oscillations are strongly reflected in the near-surface ocean temperature within the Ecuadorian Sea
- Effects of El Niño forcing are strongly influencing the Ecuadorian Sea eastward of the Galapagos Islands

Supporting Information:
- Supporting Information S1
- Supporting Information S2

Correspondence to:
T. C. Lippmann,
lippmann@ccom.unh.edu

Citation:
Marin Jarrin, M. J., & Lippmann, T. C. (2019). Interannual variability of mixed layer dynamics in the Ecuadorian Ocean. *Journal of Geophysical Research: Oceans*, *124*, 8777–8797. https://doi.org/10.1029/2019JC015086

Received 24 FEB 2019
Accepted 2 OCT 2019
Accepted article online 17 OCT 2019
Published online 11 DEC 2019

Abstract Time series spanning 22 years of monthly conductivity-temperature-depth profiles are used to examine upper water column temperature interannual variability near the Ecuador coastline. The sampling program began in 1992 (and continues) by Ecuador's National Institute of Oceanography of the Navy and National Fisheries Institute. The five coastal stations are located 8 NM away from the coast and extend from 2°S to 1°N. The anomaly data show marked interannual variations with distinct characteristics associated with El Niño Southern Oscillation (ENSO) indices. Heat content and the 20°C isotherm depth are both largest during El Niño periods and weakest during La Niña periods. The first mode empirical orthogonal function (EOF) decomposition of the anomaly coastal station data represents bulk variations of the thermocline depth and has temporal variability coupled to Niño 3.4 and 1+2 indices. Coastal observations are compared with observations obtained from the offshore TAO/Triton buoys located along 95°W from 2°S to 2°N. The EOF decomposition of TAO buoy time series shows similar spatial EOF structure. The first EOF amplitude time series from coastal and TAO station decomposition is correlated, showing that the dominant variability of the upper water column near the coast is coupled to variations along the equator and seaward of the Galápagos. Coupling between ENSO indices and ERA-1 zonal wind stress from the central Pacific (Niño 4) with observed coastal temperature structure shows that effects of El Niño forcing are strongly influencing the Ecuadorian Sea eastward of the Galápagos Islands.

1. Introduction

The importance of interannual ocean variability in the far eastern equatorial Pacific has been widely known for its relationship to fish catch in Colombia, Ecuador, Perú, and Chile (Ballón et al., 2008; Bertrand et al., 2008; Deng et al., 2013; Glynn et al., 2001); however, the details of the dynamics are not fully understood. This is particularly evident along the Ecuadorian coast where complexity arises due to the influence of equatorial dynamics in the central Pacific, upwelling variability off the coast of Perú to the south, and eastward propagating equatorial-trapped Kelvin waves, all of which contribute to the variability in the upper water column, and are thus of great importance to the economic and social development of the country (Cornejo-Rodríguez, 1987; Enfield et al., 1987; Lucero & Cornejo-Rodríguez, 1990; McPhaden, 1999; Enfield & Mestas-Nuñez, 2000; McPhaden, 2004).

The Ecuadorian Sea is located in the far eastern boundary of the equatorial Pacific, between the Galápagos triple junction and the South American plate, where the oceanic crust and lithosphere of the Nazca plate (Carnegie Ridge) begin their decent into the mantle beneath South America (Michaud et al., 2015; Figure 1). The country of Ecuador is almost evenly divided by the equator and thus occupies a somewhat unique position oceanographically where the Coriolis force goes to zero. In general, the eastern equatorial Pacific is complex, with strong influences from circulation in the Colombian Basin at low northerly latitudes (Vargas-Angel et al., 2001), the Humboldt current to the south bringing lower surface ocean temperatures northward, periodically producing coastal upwelling along the west coast of South America (Fiedler & Talley, 2006; Wade et al., 2011), as well as remotely forced, eastward propagating Kelvin waves along the equator and its interaction with the Equatorial Under Current (EUC; Cornejo-Rodríguez, 1987; Cornejo-Rodríguez & Enfield, 1987; Fiedler & Talley, 2006). This general complexity is evident in climatology of sea surface temperature (SST) derived from advanced very high resolution radiometer (AVHRR) satellite data (Reynolds et al., 2007) near the Ecuadorian Sea (Figure 2). Latitudinal gradients at the equator are present throughout the year,

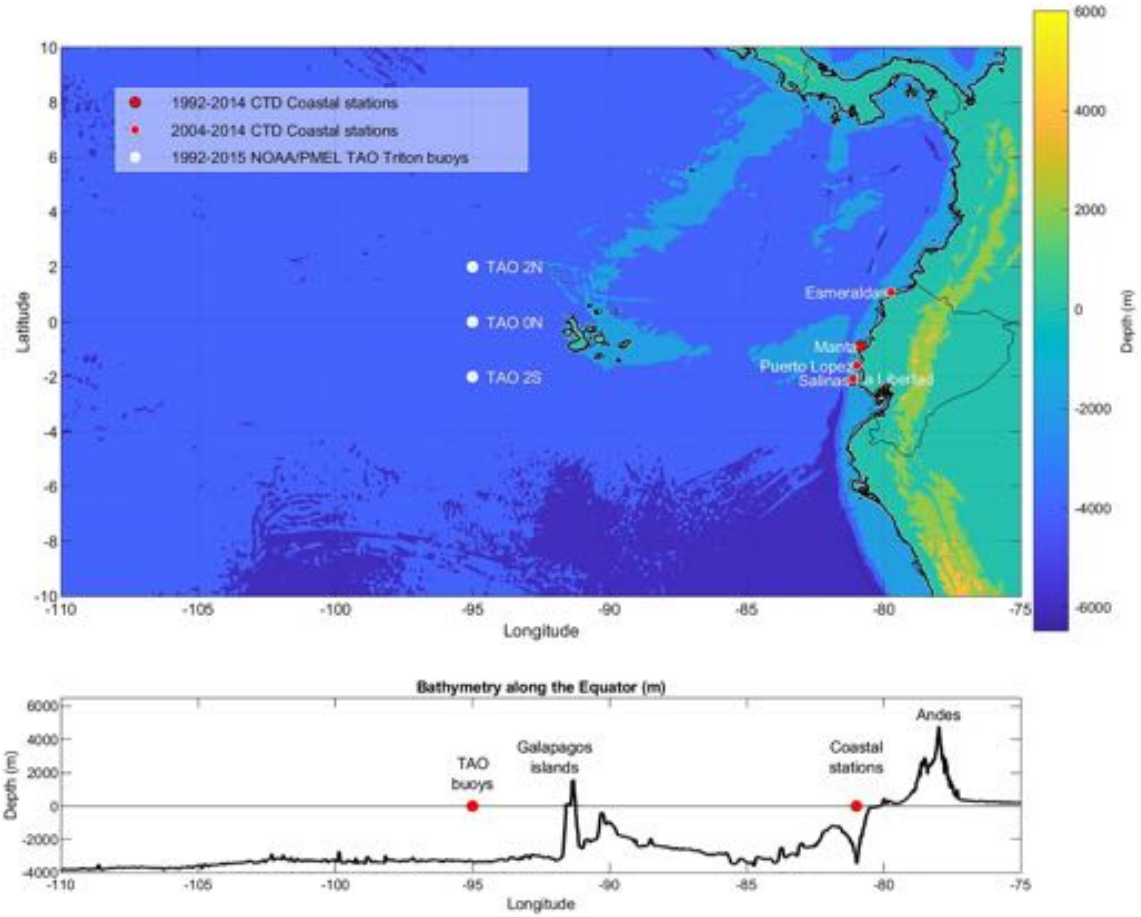

Figure 1. Upper panel: GEBCO topography/bathymetry of the study area. Coastal stations are shown in red circles, TAO buoys as white circles. Lower Panel: Bathymetric profile along the equator with TAO buoys and coastal stations as red circles.

particularly strong during the first half of the calendar year, with much higher temperatures (up to 30°C) at northern latitudes (2–10°N) than in the south (about 22°C; 2–10°S). Between July and November, the influence of the Humboldt Current (northward flowing eastern boundary current extending the length of the South American continent) appears in the surface water properties in the southern part of the Ecuadorian Sea, bringing colder surface water (blue colors in Figure 2) to the southern Ecuador coast.

Sea surface salinity climatology data (not shown) from the Aquarius satellite–obtained from the optimally interpolated sea surface salinity global dataset from 2011 to 2015 (Lee et al., 2012)–show strong latitudinal variability throughout the year and the influence of southern waters during March-August, similar to what is observed in SST climatology. Additionally, the movement of the Inter Tropical Convergence Zone (ITCZ), which influences the variability of precipitation throughout the year (Huffman et al., 2007) and oceanography in the northern Tropical Atlantic (Fiedler & Talley, 2006; Huffman et al., 2007; Lavín et al., 2006), creates a less saline pool (about 30 PSU) around 96°W, 5°N close to the Isthmus of Panamá (Morán-Tejeda et al., 2016). This ocean-atmospheric interaction influences the Ecuadorian Sea contributing to a complex, biologically diverse and somewhat unique environment (Enfield & Mestas-Nuñez, 2000). The dynamics are complicated by the presence of the Galápagos Islands, and the submarine ridge along the equator (Figure 1) connecting the islands to the mainland. Karnauskas et al. (2007) has suggested that properly including the Galápagos Islands in numerical models results in the obstruction of the EUC, as well as modifications in the simulated spatial structure of SST.

Surprisingly, few field studies have examined details of mixed layer dynamics in the Ecuadorian Sea, partially due to the lack of long term observations. However, since the recognition of the first effects

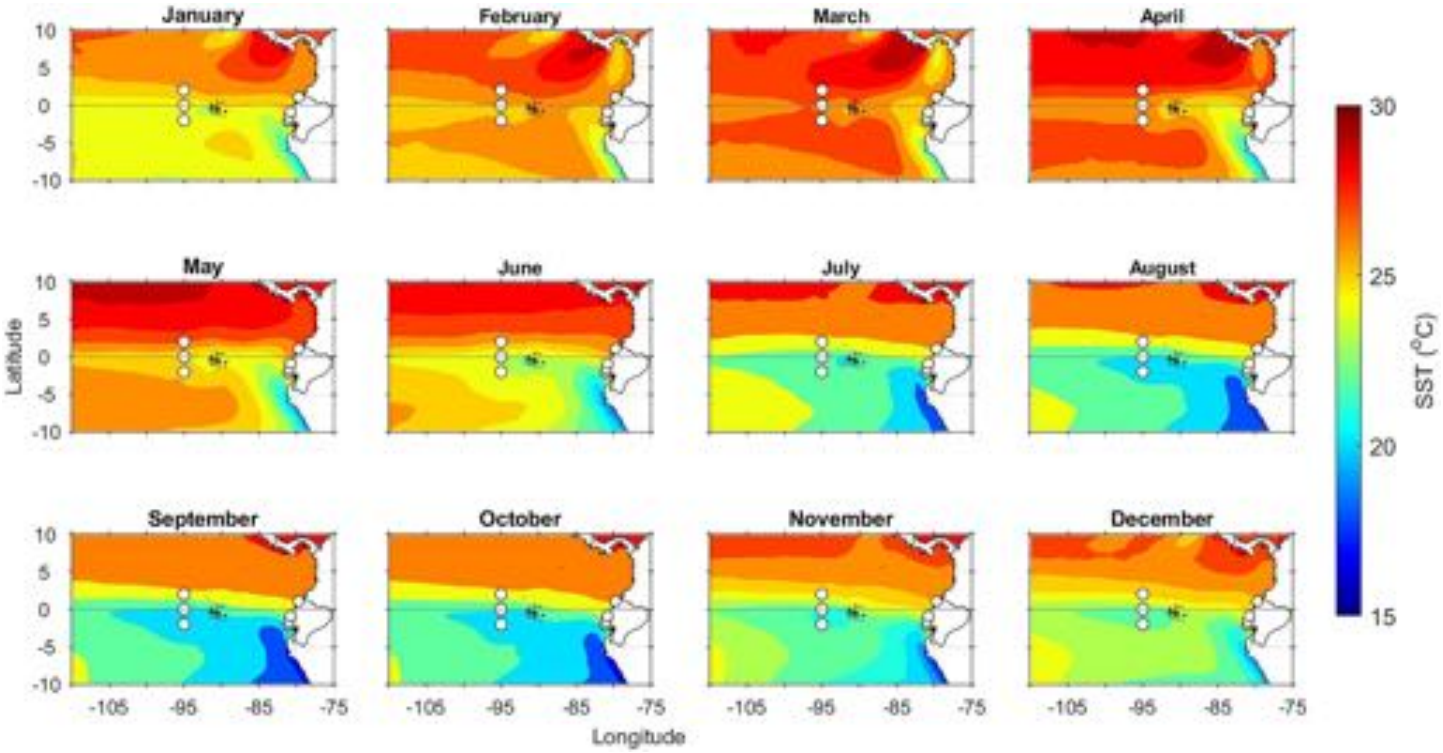

Figure 2. Sea surface temperature climatology from advanced very high resolution radiometer data spanning 1992-2015 from Reynolds et al. (2007). The locations of coastal stations are shown in dark circles and TAO buoys in white circles.

of El Niño on the area (Wyrtki, 1975), Ecuador has developed programs to sample the water column 8 NM away from the coast (Figure 1) using conductivity-temperature-depth (CTD) profilers and water samples for chemical and biological properties, as well as installing coastal and inshore meteorological stations. Monthly CTD profiles (with sampling occurring on the third or fourth week of the month) have been obtained by three Ecuadorian Research Institutes: the National Institute of Oceanography of the Navy (INOCAR), the National Fisheries Institute (INP), and the National Institute of Meteorology and Hydrology (INAMHI) since 1992 (continuing today with international cooperative agreements amongst neighboring countries) at 5 different oceanographic stations (red circles in Figure 1 and Table 1). The sampling sites were established in 1992 by the 3 institutions, and located 8 NM from the coast for logistical convenience close to known productive fish-catch areas (http://cpps-int.org/).

The purpose of this work is to evaluate the long time series of observations obtained at the Ecuadorian coastal stations and to examine the interannual variability in the surface mixed layer hydrography observed near the Ecuador coast over the 22-year record length. Owing to limitations in the observed salinity records and the generally small variation in upper ocean salinity of this area, temperature profiles will be primarily used to quantify surface layer variability. Analysis will be on anomaly time series whereby the climatological (seasonal) signal has been removed, and further be restricted to the upper 100 m of the water column due to typical CTD cast depths. Several parameters that characterize mixed layer variability will be computed, including the depth of the 20°C isotherm, integrated (over the vertical) heat content, and amplitude time series from dominant modes of an orthogonal decomposition (empirical orthogonal function [EOF]) of the climatology-corrected (anomaly) data. We will examine the relationship between equatorial coastal ocean upper water column temperature variability with temperature profile time series observed to the west of the Galápagos Islands along the equator but outside the Ecuadorian Sea, El Niño Southern Oscillation (ENSO) indices derived from satellite SST in the central Pacific, remote forcing by zonal wind stress across the equatorial Pacific, and regional winds derived from European Centre for Medium-Range Weather Forecasts (ECMWF) reanalysis.

Table 1
Location (Fraction Degrees), Dates, Number of Samples, and Monthly Temperature (°C) Maxima, Minima, and Standard Deviation From Coastal Oceanographic Stations and TAO Buoys

Name of station	Latitude (°N)	Longitude (°E)	Dates of survey	Number of data sets	Temperature monthly anomaly		Standard deviation
					Max.	Min.	
Monthly coastal CTD stations							
Esmeraldas (INP)	1.08	−79.74	2004 to 2014	95	8.10	−8.61	1.69
Manta (INOCAR)	−0.88	−80.83	1992 to 2014	219	9.57	−7.87	1.89
Puerto López (INP)	−1.59	−80.99	2004 to 2014	90	4.48	−5.20	1.28
La Libertad (INOCAR)	−2.07	−81.12	1992 to 2014	293	9.79	−6.20	1.92
Salinas (INOCAR)	−2.12	−81.13	2004 to 2014	60	6.54	−6.17	1.44
Daily TAO Project (NOAA/PMEL) buoys							
TAO 2N	2.00	−95.00	1992 to 2015	8248	12.55	−6.99	1.71
TAO 0N	0.00	−95.00	1992 to 2015	8257	11.52	−5.89	1.76
TAO 2S	−2.00	−95.00	1992 to 2015	8196	10.83	−5.84	1.43

Abbreviations: CTD: conductivity-temperature-depth; INOCAR: National Institute of Oceanography of the Navy; INP: National Fisheries Institute; NOAA: National Oceanic and Atmospheric Administration; PMEL: Pacific Marine Environmental Laboratory.

2. Materials and Methods

2.1. Field Observations: Coastal In Situ Data

Periodic sampling approximately 8 NM away from the coast was done using convenience vessels such as small fishing boats, pleasure craft, and Ecuadorian military ships. The SeaBird Electronics (SBE) CTD 19 and 19plus were used to obtain temperature and salinity depth profiles. Instruments were sent back to SBE about every two years for calibration. All CTD cast data were processed using software provided by SBE, filtered with a low-pass spatial filter, and further aligned relative to pressure (based on instrument response time). Data were not considered when the profiler was moving upwards. Temperature and salinity were averaged to evenly spaced 1-m depth bins using SBE's software. Profile data were further filtered with temperature/salinity diagrams by manually eliminating those data points outside of the expected range (outliers) determined with a three standard deviation filter. Months with more than one sample were averaged, and all monthly samples at all stations were given a time stamp centered to the 15th of each month.

Time series of temperature profiles for each coastal station are shown in Figure 3. Gaps in the data arise from poor CTD data, missed sampling times, or instrument malfunction. As expected the data reveal a clear seasonal variability with generally a deeper pool of surface warm water during the rainy season (April–August), similar to SST climatology (Figure 2). Present also are longer time scale variations associated with (sometimes) strong interannual (or episodic) events. The 20°C isotherm, extensively used previously to characterize surface heating and cooling in the upper water column (Chavez et al., 1999; McPhaden, 2012) is indicated in the figure. During years of high surface heating (or reduced upwelling), the 20°C isotherm was not always present in the temperature profiles above 100 m (e.g., 1997–1998).

As an alternative, the surface layer variability can be parameterized by the thickness of the mixed layer depth (MLD), as suggested by Thomson and Fine (2003) and Jeronimo and Gomez-Valdes (2010). MLD was determined for each profile by searching for a temperature value differing by more than 0.5°C from the near-surface reference level, defined as 5 m below the surface due to influence of high frequency variability right at the surface [following de Boyer Montégut et al., 2004]. However, MLD depths less than 5 m and greater than 100 m could not be determined, and the possible presence of fossil mixed layers (Sprintall & Roemmich, 1999) where observed in the time series which contributed uncertainty in identifying a single representative MLD in any given profile. As a consequence, MLD is not considered further in the analysis.

A second method was considered based on heat content (HC; in J/m^2), an often used proxy for the deepening or shallowing of the western Pacific thermocline depth (Wyrtki, 1981), defined by Dijkstra (2008) as

$$H_C = C_p \int_{-H_f}^{0} \rho T \; dz \tag{1}$$

where H_f is a fixed reference depth (chosen herein as 100 m due to the constraints of the observed temperature profiles), C_p is the heat capacity for seawater calculated using United Nations Educational, Scientific

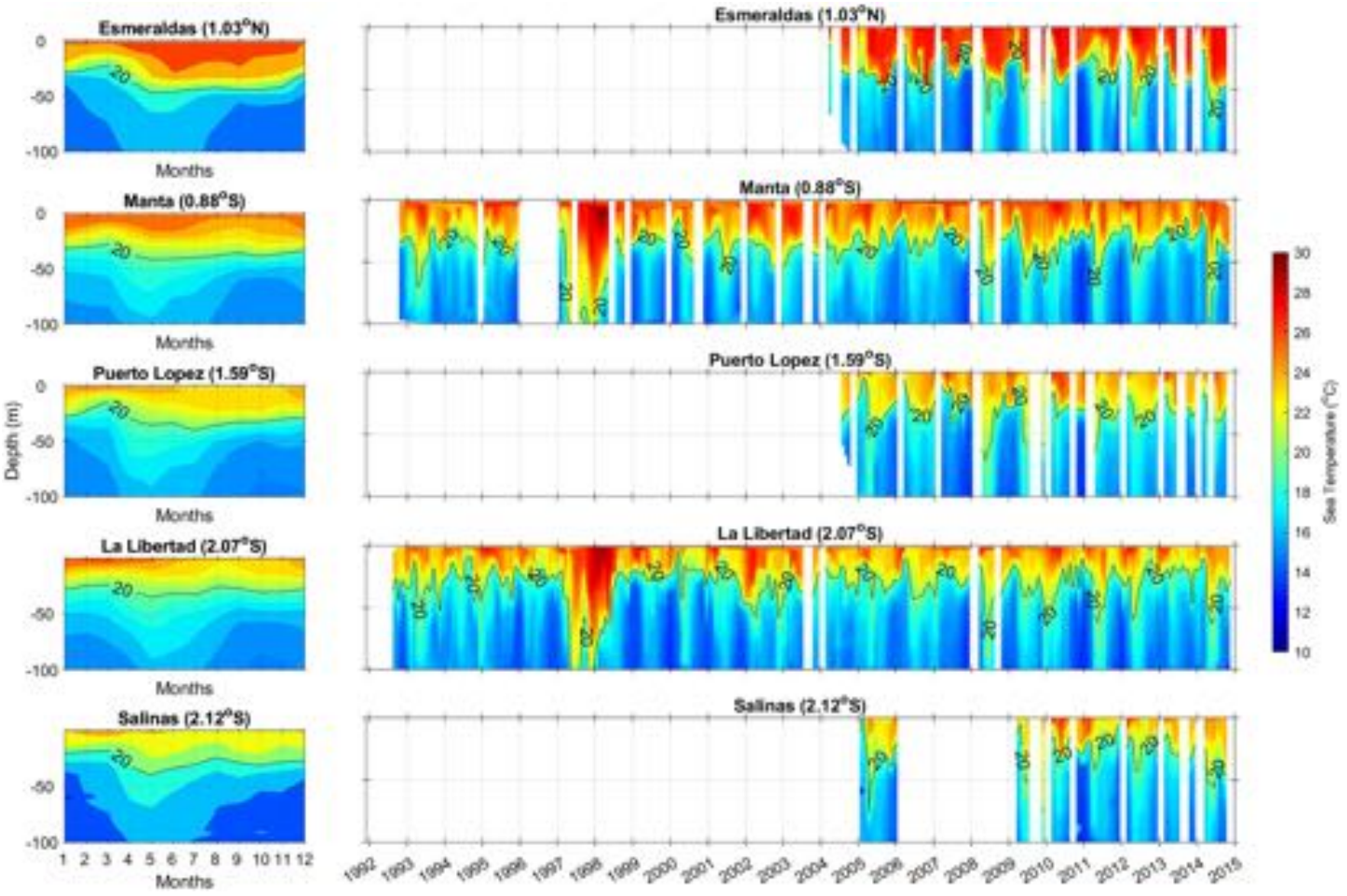

Figure 3. (Left panels) Temperature climatology as function of water depth for each coastal station (station name and latitude indicated in each panel). (Right Panels). Time series of temperature profiles for each station. The 20°C isotherm is shown as a black contour in all panels. Colors represent temperature with scale bar shown on the right.

and Cultural Organization (UNESCO) 1983 polynomial formula, and ρ is density of the water calculated using UNESCO 1983 (EOS 80) polynomial from observed temperature and salinity profiles (Fofonoff & Millard, 1983). HC represents an integrated (over depth) value of total heat contained in the upper water column that is relatively insensitive to the shape of the temperature profile.

Monthly climatology was determined for temperature, salinity, and heat content by averaging all data for any given month over the 22-year record. Climatological monthly sea temperature profiles as a function of depth at the coastal stations (Figure 3) show that from April to August most of the water column is warmer than the rest of the year, with a slight-apparent deepening of the 20°C isotherm, quite similar to that observed in SST climatology (Figure 2). The most southerly station (La Libertad at 2.03°S; Table 1) shows a stronger influence of colder waters in August than that observed in Manta (located closer to the Equator at 0.86°S; Table 1). The most northerly station (Esmeraldas at 1.08°N) shows warmer surface waters than the more southerly stations, possibly due to high influence from the Colombian Basin. The shorter-record stations (Esmeraldas, Puerto López and Salinas, located at 1.08°N, 1.59°S, and 2.12°S; Table 1) show similar variability in time and depth; however, due (possibly) to the shorter record length (11 years; Table 1), the general climatology appears to be colder than stations with longer time series (22 years; Table 1). Despite the proximity to the coast, HC and depth of the 20°C isotherm time series suggests that the coastal stations located 8 NM from the coast represent the general characteristics of the area without major influence by terrestrial freshwater runoff or the principal Guayas and Esmeraldas rivers with average discharge of 835 m^3/s and 608 m^3/s, respectively (U.S. Army Corps of Engineers, 1998).

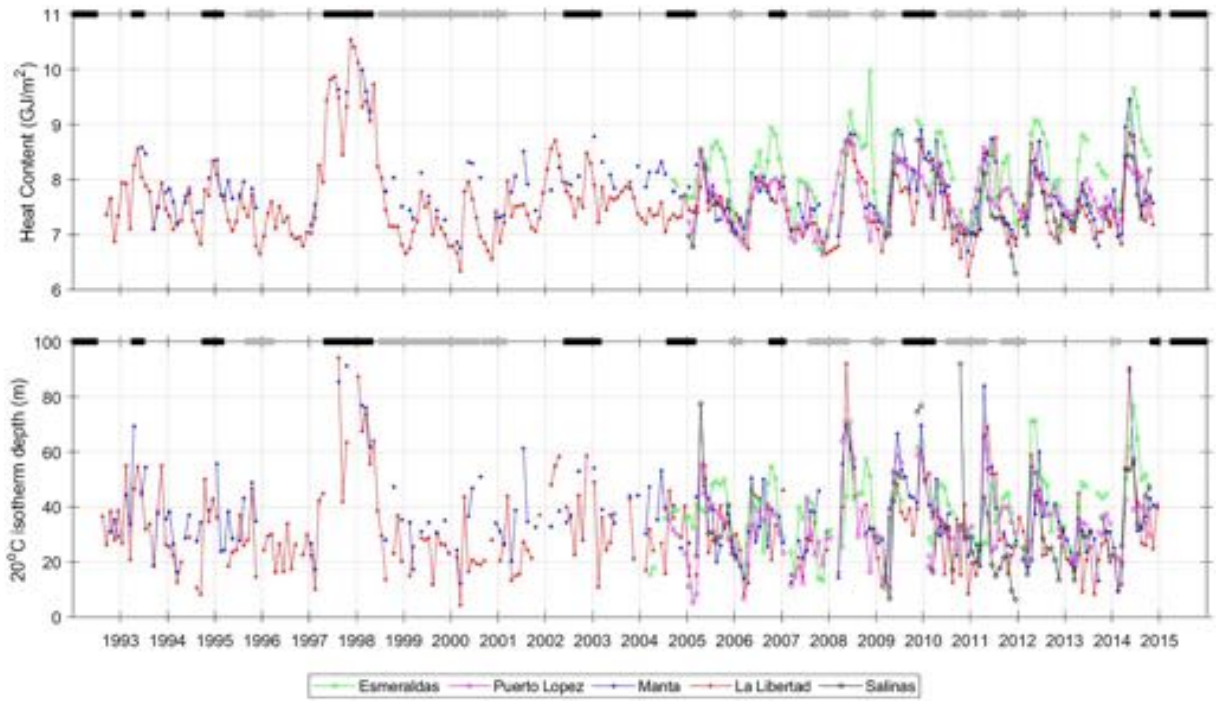

Figure 4. Heat content (upper panel) and 20°C isotherm depth (lower panel) time series from each coastal station. Missing data are due to profiles that do not extend to depths of 100 m, where the 20°C contour is greater than 100 m, or there is no salinity data. The black squares on top denote warm events and gray squares denote cold events, based on 3-month running mean of ERSST.v4 sea surface temperature anomalies in the Niño 3.4 region.

Our interests are in understanding the interannual variability that differs from the seasonal signal. That is, we seek to identify the nature of the variability that differs from the climatology. To eliminate the seasonal cycle from the data, we subtract the climatology from the time series at each station, henceforth referred to as the "anomaly" time series.

Anomaly time series of the 20°C isotherm and HC for all stations were determined by subtracting their respective climatology from the observations and are subsequently used to assess the interannual variability of the upper water column (Figure 4). Time series of the 20°C isotherm at Manta and La Libertad were quite similar, with depth ranges of 10–96 m, and 6–93 m, respectively (Table 2). The 20°C isotherm depth varied synchronously (0 lag) with temperature fluctuations at a depth of 5 m below the surface with correlations, R, ranging 0.40–0.49 for the long records (Manta and La Libertad) and 0.59–0.79 at the shorter stations (Esmeraldas, Puerto López, and Salinas). The 95% significance level (ranging 0.18–0.32) was determined by the bootstrap method described in Ebisuzaki (1997). HC also shows strong interannual variability similar to the 20°C isotherm depth ($R > 0.27$ and $R > 0.65$ at the short and long records, respectively). In general, the 20°C isotherm depth and HC seem to follow each other reasonably closely.

Table 2
Maxima, Minima, and Standard Deviation of Depth of 20°C Isotherm and Heat Content From the Coastal Stations and TAO Buoys

	Depth of 20°C isotherm (m)			Heat content (GJ/m^2)		
Station	Min.	Max.	SD	Min.	Max.	SD
Esmeraldas	6	80	13.30	8.8	9.7	0.67
Manta	10	96	20.93	6.7	10.5	0.68
Puerto López	8	74	13.07	1.1	8.6	0.46
La Libertad	4	93	21.29	6.3	10.5	0.69
Salinas	8	58	16.98	3.4	8.4	0.52
TAO buoy 2°N	21	92	15.15	6.9	11.3	0.71
TAO buoy 0°N	3	95	20.84	5.9	11.3	0.93
TAO buoy 2°S	2	98	20.15	6.2	11.3	0.89

2.2. Field Observations: TAO Buoy Data

Three surface and subsurface buoys from the Tropical Atmosphere Ocean - Triangle Trans-Ocean Buoy Network (TAO/Triton) in the Pacific (McPhaden et al., 1998), west of the Galápagos at 95°W, were used for comparison to the coastal stations (Table 1). Observations from TAO/Triton buoys included temperature at "standard depths" of 1, 5, 10, 15, 20, 40, 50, 60, 75, 80, and 100 m, sea surface salinity, and winds (4 m above sea level). Heat content here was obtained from data between depths ranging 1–100 m by using a constant salinity of 35 PSU over the water column (errors in HC using this assumption are negligible) (Levitus et al., 2012).

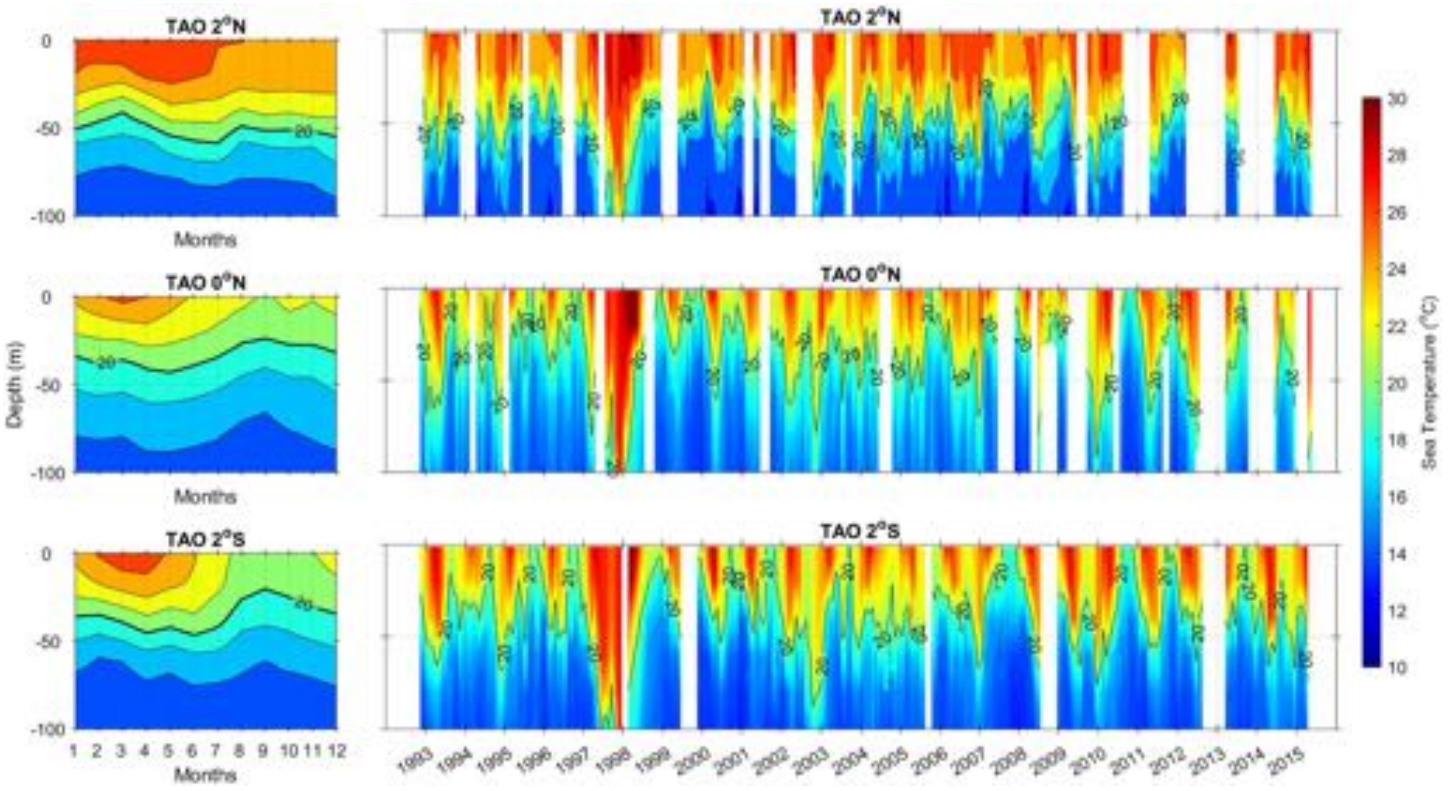

Figure 5. (Left panels) Temperature climatology as function of water depth for each TAO buoy (latitude indicated in each panel). (Right panels) Time series of temperature profiles for each buoy. The 20°C isotherm is shown as a black contour in all panels. Colors represent temperature with scale bar shown on the right.

Time series of temperature profiles from TAO buoys are shown in Figure 5 over the same time period as the observations of the coastal station data (Figure 3). As with the coastal data, there is a strong seasonal cycle with the same monthly pattern. The surface temperatures at the southern buoy are generally colder during the second half of the year than that observed in the northern buoy. TAO buoy climatological monthly sea temperature profiles as a function of depth (Figure 5) show a slighter warming of the water from April to August compared to the coastal stations, with a slight-apparent deepening of the 20°C isotherm (shown in black) most noticeable in the equatorial and southern buoys. Stronger influence of cold waters beneath 80-m depth may be due to the influence of the EUC in waters west of the Galápagos Islands.

Figure 6 shows the 20°C isotherm depth and HC for each of the TAO buoys. The 20°C isotherm at the 2°N buoy remains under 40-m depth, while at the other two buoys (at the Equator and 2°S) this isotherm may reach up to 20-m depth during the second half of the year. HC time series were calculated using equation (1) while accounting for the unequal depth locations of the instruments by linearly interpolating each profile to constant 1-m depth increments. Density was determined from temperature profiles and a constant salinity value observed at the surface. These time series qualitatively show similar behavior as the coastal stations (Figure 3). Cross correlation between HC at the La Libertad coastal station and the TAO buoy data shows most similarity with the southern buoy ($R > 0.75$) occurring at 0 lag, while at Manta, the maximum correlation with TAO 2°S ($R = 0.80$) and TAO 0°N ($R = 0.68$) occur at 1-month lag, and at TAO 2°N ($R = 0.72$) occur at 0 lag, with 95% significance level of 0.16–0.21 determined from methods described by Ebisuzaki (1997).

Analysis of surface layer variability using heat content or 20°C isotherm require predetermined parameters (depth limits, temperature value) making the results subject to somewhat arbitrary choices, often determined by limitations of the data sampling. To better objectively represent the surface layer variability measured by temperature profiles across all 5 coastal stations, the array time series, $\boldsymbol{X}(\mathbf{x}_m, \boldsymbol{t})$, where $\mathbf{x}_m = \boldsymbol{f}(\boldsymbol{x},\boldsymbol{z})$, x is horizontal location of the stations, z is depth, and t is time, can be decomposed into an ordered set of M

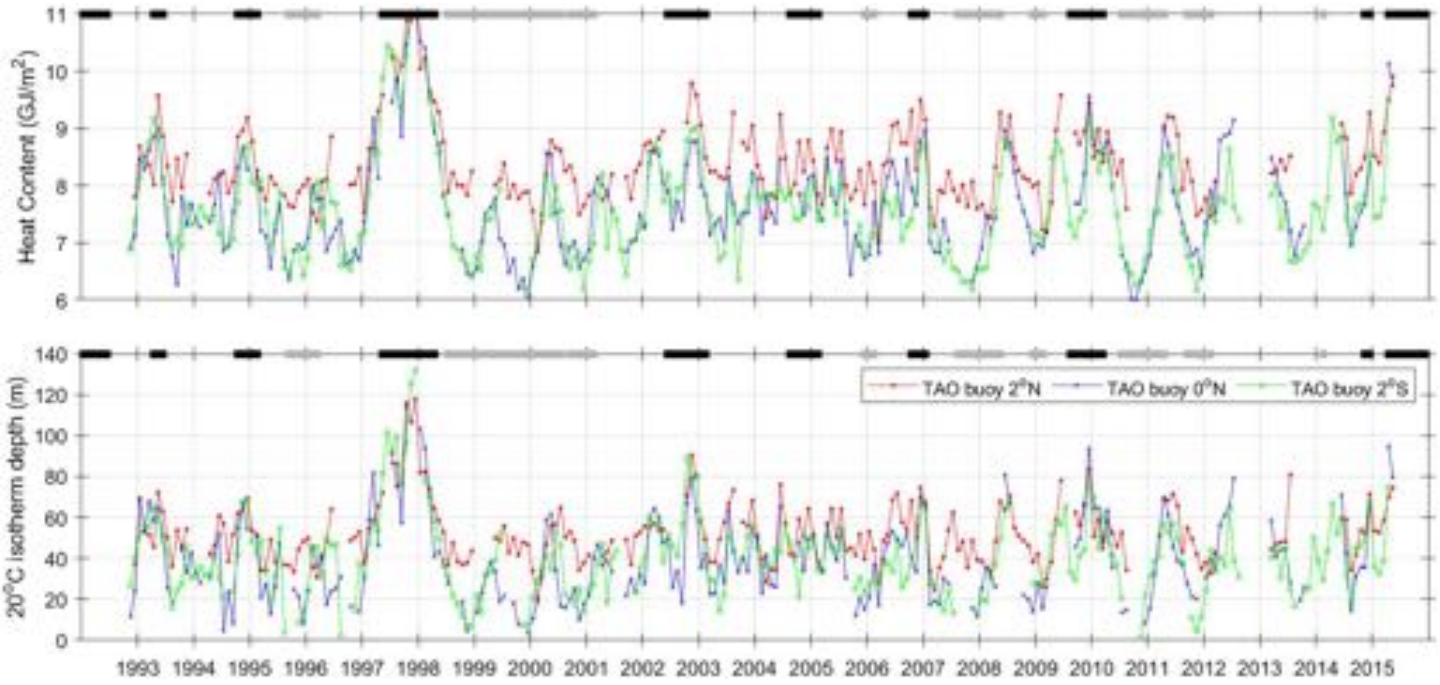

Figure 6. Heat Content (upper panel) and 20°C isotherm depth (lower panel) time series from each TAO buoy. Missing data are due to profiles that do not extend to depths of 100 m, where the 20°C contour is greater than 100 m, or there is no salinity data. The black squares on top denote warm events and gray squares denote cold events, based on 3-month running mean of ERSST.v4 sea surface temperature anomalies in the Niño 3.4 region.

orthogonal functions (or EOF modes equal in number to the number of sampled locations in both horizontal and vertical dimensions) that span the variability in the most efficient manner, such that

$$X(\mathrm{x}_m, t) = \sum_{j=1}^{M} A_j(t) F_j(\mathrm{x}_m) \tag{2}$$

where $\boldsymbol{F_j(\mathrm{x}_m)}$ are the normalized eigenvectors for mode j, and the EOF amplitude time series (or temporal weighting), $\boldsymbol{A_j(t)}$, are given by,

$$A_j(t) = \sum_{m=1}^{M} F_j(\mathrm{x}_m) X(\mathrm{x}_m, t) \tag{3}$$

The EOF modes are ordered in terms of the amount of variance explained with the first mode describing the highest fraction of variance. Physical interpretation of successively higher modes is difficult owing to the possibility of sampling errors influencing the separation of modes in the decomposition of the data (North et al., 1982).

The two long record coastal stations (La Libertad and Manta) span 22 years, whereas the three short records (Esmeraldas, Puerto López, and Salinas) span only 11 years. In order to encompass the longest time series and better evaluate the interannual variability, we will use the long record anomaly time series as our primary input to the EOF analysis. However, we will also compare the EOF decomposition from the long records with an EOF decomposition of all five stations but only for the overlapping portions (11 years). This allows and assessment of the impact that the spatial extent of the stations—larger for the short records and extending north of the equator—has on the interpretation of the results.

3. Results

Figure 7 shows the spatial eigenvectors, $F_j(\mathrm{x}_m)$, of the first three modes, $j = 1,2,3$, and their corresponding amplitude time series, $A_j(t)$, resulting from EOF decomposition of the anomaly time series, $X(\mathrm{x}_m, t)$, using only the longest two records of the coastal station data (that obtained at La Libertad and Manta). The spatial function of the first mode EOF, $F_1(\mathrm{x}_m)$, accounting for 70.9% of the variance, shows that most of the

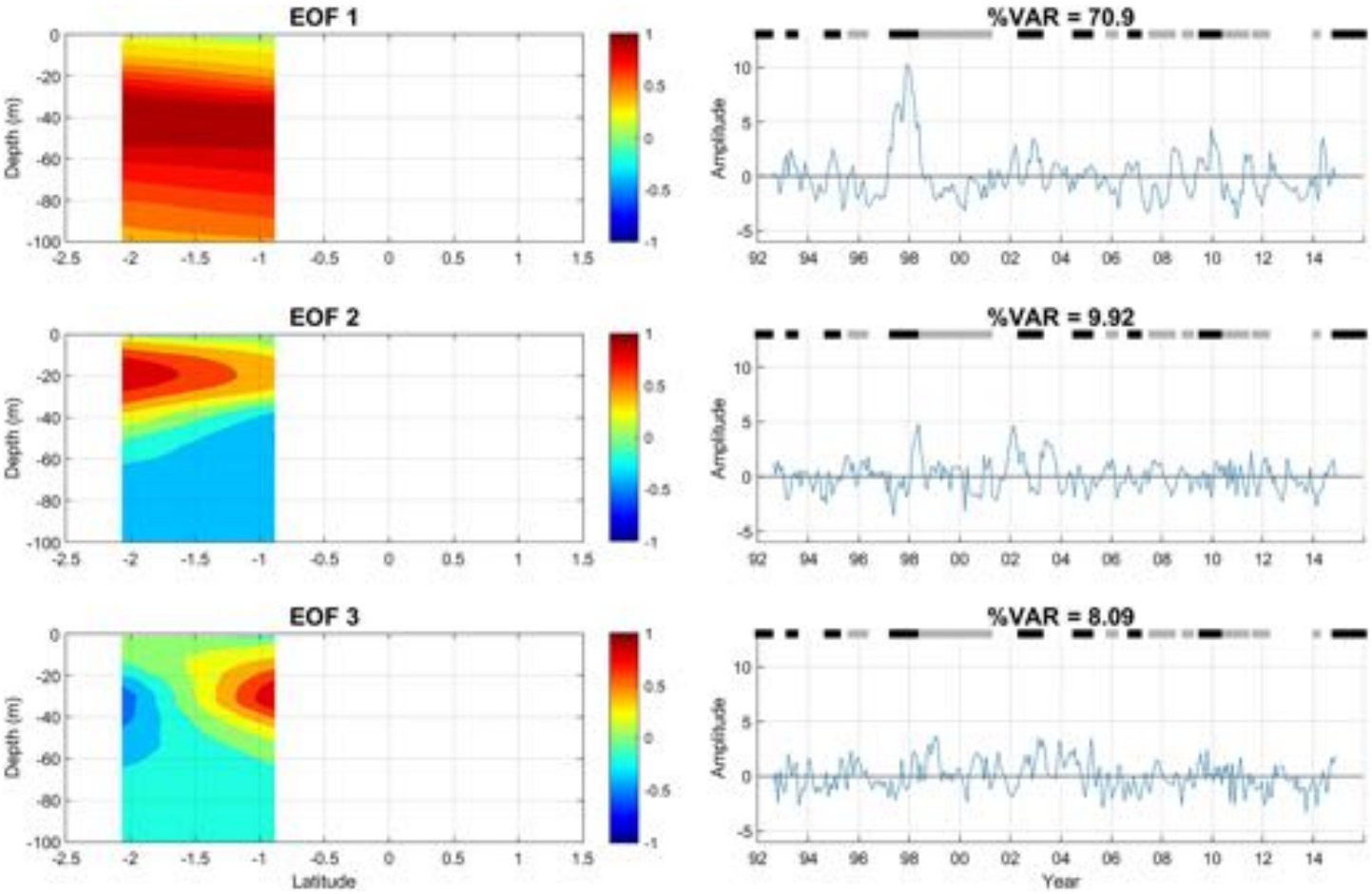

Figure 7. (Left panels) First 3 spatial empirical orthogonal function (EOF) modes from analysis of temperature anomaly coastal station data at La Libertad and Manta (long records). EOFs are shown as a function of depth and latitude, and are normalized to have a maximum absolute value of 1. (Right panels) The corresponding EOF amplitude time series for the first three modes. The fraction of variance explained by each mode is shown on each panel. The black squares on top denote warm events and gray squares denote cold events, based on 3-month running mean of ERSST.v4 sea surface temperature anomalies in the Niño 3.4 region.

variability of the temperature anomaly is centered around 40-m depth where the average base of the thermocline is found. The amplitude time series, $A_1(t)$, show substantial interannual variation, with differences from the climatology up to 10°C (occurring in 1997–1998; Figure 7). The second and third modes, $F_2(\mathrm{x}_m)$ and $F_3(\mathrm{x}_m)$, account for 9.9% and 8.1% of the variance and qualitatively describes vertical and horizontal (latitudinal) deviations from the basic thermal structure defined by the thermocline (EOF 1). The corresponding amplitude time series, $A_2(t)$ and $A_3(t)$, show lower amplitude variations and are markedly different from $A_1(t)$. The spatial structure in $F_j(\mathrm{x}_m)$ of the first three modes shows that most of its variability is contained in the mixed layer (as expected). Higher modes ($j > 3$) in all data sets each independently represent no more than 3% of the variance and are not considered.

Figure 8 shows results of the EOF decomposition including anomaly data from all of the coastal stations, but limited in temporal extent to the duration of the short records (11 years dating back to 2004). The first three EOF modes, $F_j(\mathrm{x}_m)$ for $j = 1,2,3$, and their corresponding amplitude time series, $A_j(t)$, account for 44.2%, 13.4%, and 8.1% of the variance, respectively. The spatial structure of the first EOF mode, $F_1(\mathrm{x}_m)$, from these data is quite similar to that when using only the 2 stations with the longest records (Figure 7). The general nature of the second and third mode EOFs, $F_2(\mathrm{x}_m)$ and $F_3(\mathrm{x}_m)$, is not as similar in spatial structure, and contains qualitatively more latitudinal variation.

Higher modes (2 and 3) have lower amplitude and smaller time scale variability, and may be due to local ocean processes unrelated to larger scale ocean variability such as coastal winds, or in the case of the

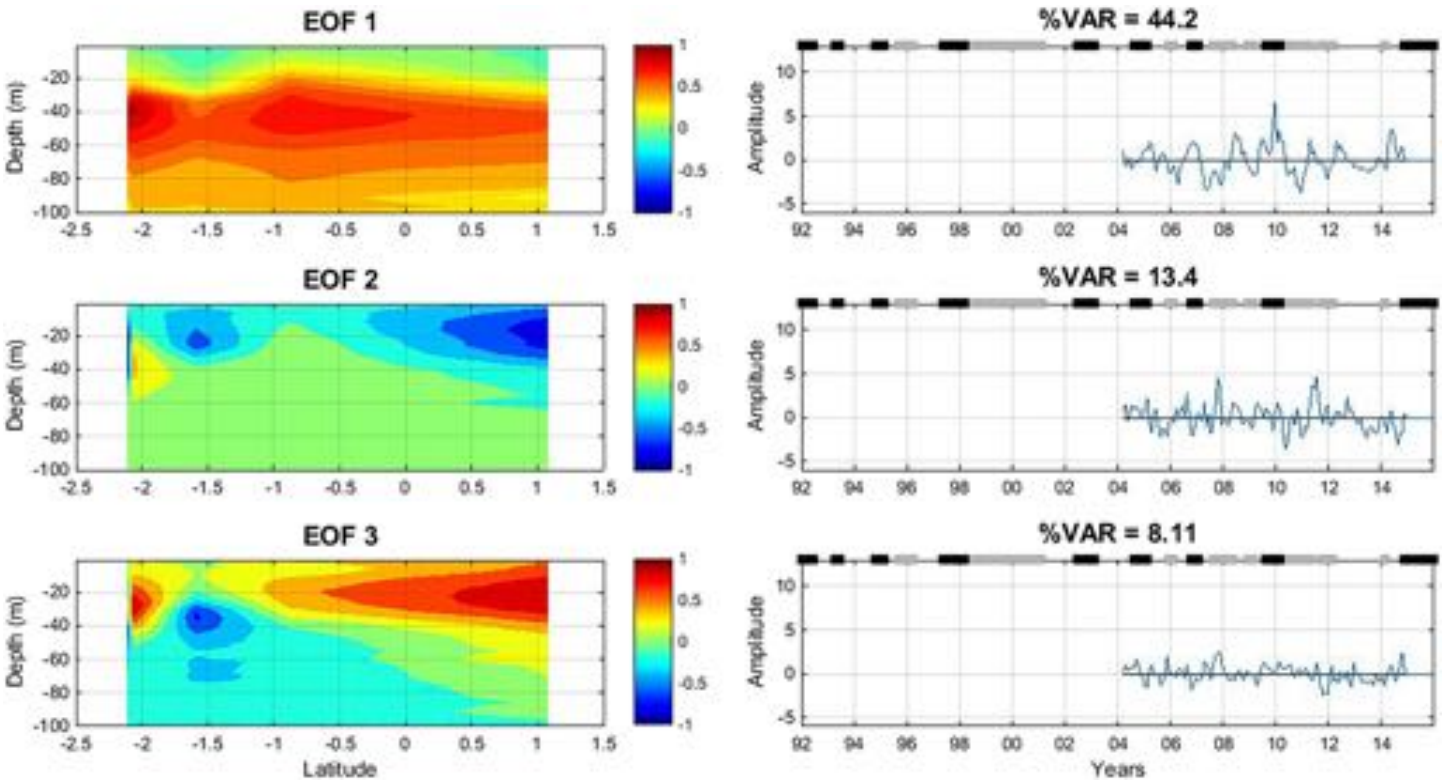

Figure 8. (Left panels) First 3 spatial empirical orthogonal function (EOF) modes from analysis of temperature anomaly at all coastal stations data from 2004 to 2014 (length of shorter records). EOFs are shown as a function of depth and latitude, and are normalized to have a maximum absolute value of 1. (Right panels) The corresponding EOF amplitude time series for the first three modes. The fraction of variance explained by each mode is shown on each panel. Black squares on top denote warm events and gray squares denote cold events, based on 3-month running mean of ERSST.v4 sea surface temperature anomalies in the Niño 3.4 region.

coastal stations may be susceptible to aliasing from short duration storm events. It should also be noted that the higher modes explain fractions of variance that are not well separated. North et al. (1982) discuss the effects of sampling errors of EOF decomposition, and provide a simple method for determining if successive modes have eigenvalues that are sufficiently separated (shifted) to be distinguishable from sampling errors. The shift is determined by $(2/N)^{1/2}$, where $N = 79.3–37.5$ is the number of independent observations estimated following Chelton (1983) corresponding to 95% significant levels ranging 0.22–0.32, respectively. This results in separation of modes based on variance explained ranging 15.9–23.1%. This range suggests that the first mode EOF is separable from the second mode, but that higher modes likely are affected by sampling errors such that adjacent EOFs have structure that is mixed relative to the true decomposition. As a consequence, higher modes 2 and 3 are not discussed further.

A comparison of the first EOF amplitude time series, $A_1(t)$, between the long and short record EOF decompositions is shown in Figure 9. The significant level is based on the bootstrap method of Ebisuzaki (1997) using 10000 time series with the same amplitude power spectra but with random phases as the input time series. Results indicate that the first mode EOF amplitude time series, $A_1(t)$, from each decomposition are significantly correlated ($R = 0.95$; occurring at zero lag). The strong correlation between $A_1(t)$ of the long and short record decomposition shows that the longer record $A_1(t)$—resulting from decomposition of only two coastal stations—behaves similarly to the short record $A_1(t)$ that results from decomposition of all 5 coastal stations. Considering that the dominant spatial EOFs, $F_1(x_m)$, from each decomposition are similar, also suggests that the first mode amplitude time series, $A_1(t)$, of the long record decomposition should contain the bulk variability of the thermocline representative of the coastal stations as a whole.

The variability of the upper water column observed by the coastal stations is compared with temperature profiles obtained from TAO buoys just to the west of the Galápagos, outside the geographic boundaries of the Ecuadorian Sea, and open to unimpeded influence from the central Pacific. As with the coastal station

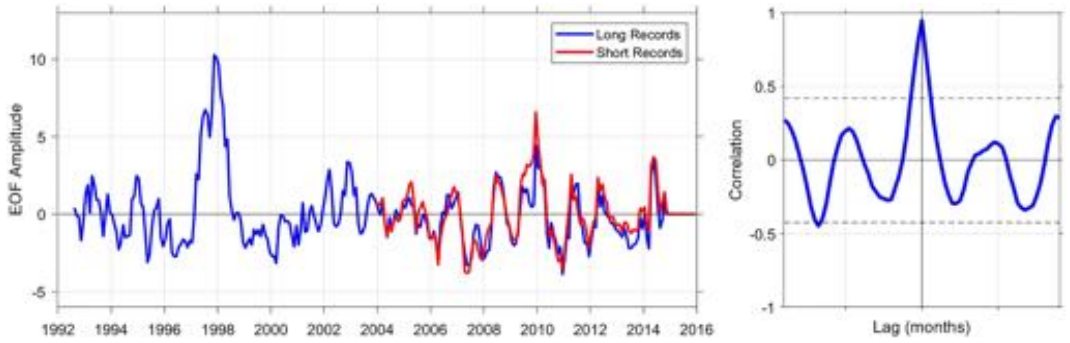

Figure 9. (Left panel) Comparison of empirical orthogonal function (EOF) amplitude time series from the analysis of the short (red) and long (blue) records. (Right panel) Lagged cross correlation between EOF 1 from the long record with EOF 1 from the short record. 95% significance level is shown as dashed lines determined by methods described in Ebisuzaki (1997).

records, we subtract the climatology from the filtered TAO buoy data and decompose these anomaly time series into orthogonal EOF modes (using Eq. (2) and (3)). Figure 10 shows the first three spatial EOF modes, $F_j(x_m)$ for $j = 1,2,3$, and their corresponding amplitude time series, $A_j(t)$. These modes are directly comparable to that obtained for the long record coastal station data (Figure 7). The first spatial EOF

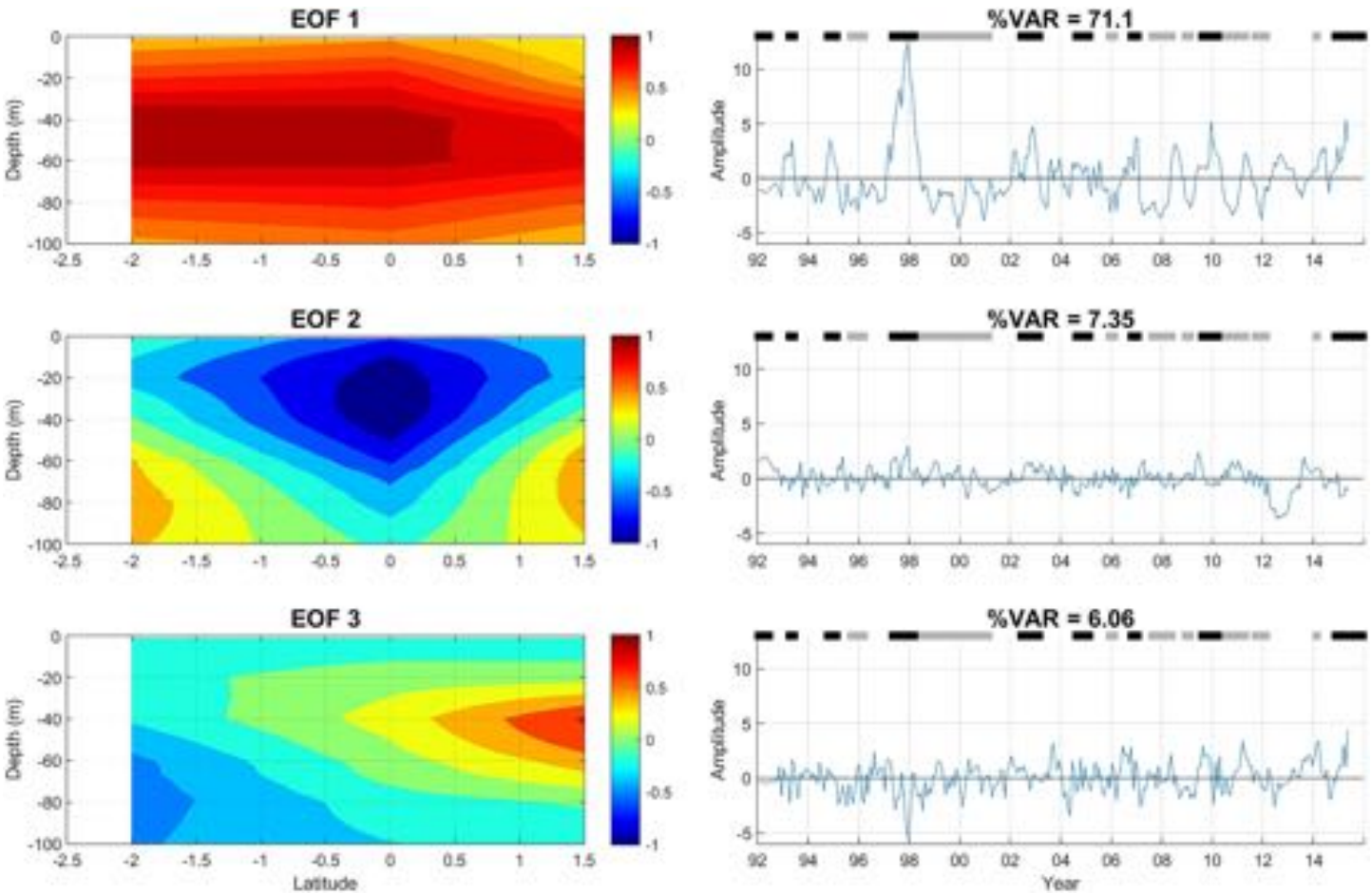

Figure 10. (Left panels) First 3 spatial empirical orthogonal function (EOF) modes from analysis of temperature anomaly at all TAO buoys. EOFs are shown as a function of depth and latitude, and are normalized to have a maximum absolute value of 1. (Right panels) The corresponding EOF amplitude time series for the first three modes. The fraction of variance explained by each mode is shown on each panel. The black squares on top denote warm events and gray squares denote cold events, based on 3-month running mean of ERSST.v4 sea surface temperature anomalies in the Niño 3.4 region.

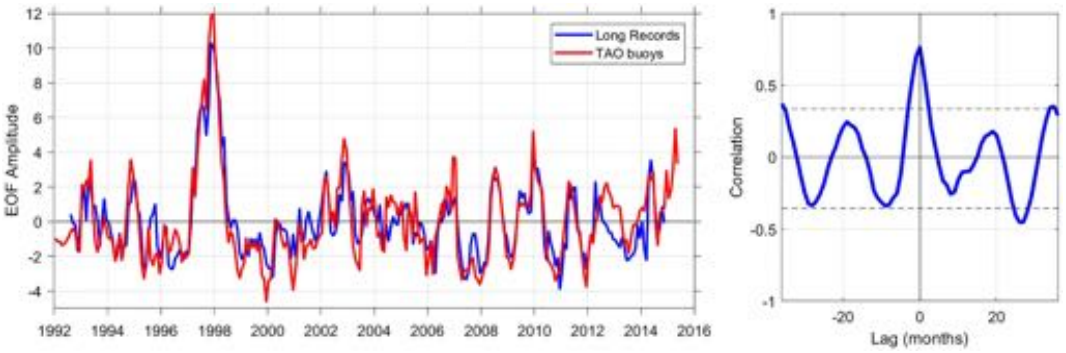

Figure 11. (Left panel) Comparison of empirical orthogonal function (EOF) amplitude time series from the analysis of the coastal stations (long record in blue) and TAO buoy (red) data. (Right panel) Lagged cross correlation between EOF 1 from the long record coastal stations with EOF 1 from the TAO buoy data. 95% significance levels are shown as dashed lines determined by methods described in Ebisuzaki (1997).

mode, $F_1(x_m)$, of the TAO buoys, accounting for 71.1% of the variance, represents deviations in temperature from the climatological mean thermocline (with approximate mean thermocline at about 50 m depth), and varies nearly uniformly horizontally across the equator. This behavior is very similar to $F_1(x_m)$ from the coastal station data (Figure 7), although the maximum variation in $F_1(x_m)$ is about 10 m deeper at the TAO stations. The corresponding amplitude time series for the first mode, $A_1(t)$, from TAO data also shows very similar temporal variability and magnitude as the coastal station data, with maximum deviation from the climatological mean of 11°C occurring during the 1997–1998 time period. The second and third EOFs, $F_2(x_m)$ and $F_3(x_m)$, contain variability (10 and 9%, respectively) latitudinally about the equator and vertically relative to the first spatial mode $F_1(x_m)$. The amplitude time series from the second and third modes, $A_2(t)$ and $A_3(t)$, show limited distinguishable energetic events. Analysis of sampling errors following North et al. (1982) also shows that TAO modes 2 and 3 are not distinguishable from sampling errors, and are also not considered further.

A comparison of the first EOF amplitude time series, $A_1(t)$, from the decomposition of the anomaly data from the coastal station long records (close to shore) and the TAO buoys (west of the Galápagos) are shown in Figure 11. Qualitatively, the time series from the first EOF mode, $A_1(t)$, are very similar. Lagged cross-correlations between the corresponding $A_1(t)$ from the two locations are also shown in Figure 11. The first mode, $A_1(t)$, between the coastal stations and TAO buoy locations are significantly correlated with maximum correlation (R = 0.86) occurring at zero lag. This suggests that the bulk (about 74%) of the variance in $A_1(t)$ of the temperature profile anomaly observed in the long record coastal stations is explained by similar observations west of the Galápagos.

4. Discussion

4.1. ENSO

Widely known ENSO indices derived in the central Pacific Ocean were compared to the anomaly data from the coastal stations and TAO buoys to determine if the variability in the coastal Ecuadorian Sea is impacted by larger scale processes. ENSO indices are prominently used to quantify strong interannual variability in the central equatorial Pacific and are commonly defined based on satellite-derived SST anomalies in the 3.4 El Niño region between 5°N–5°S, 170°W–120°W, and in the 1+2 region (0°–10°S, 90°W–80°W), closest to the study area (Figure 12; Rasmusson & Carpenter, 1982; Huang et al., 2015). Figure 12 shows the time series of Niño 3.4 and Niño 1+2 regions, spanning the duration of the study (1992–2014). Both ENSO time series were compared to the EOF 1 amplitude time series, $A_1(t)$ (equation (3)), of the anomaly data at both the coastal stations and the TAO buoys (shown later in Figure 14). El Niño (warm) episodes are determined in various ways, and herein defined as five consecutive 3-month running mean SST anomalies that exceed a 0.5°C threshold in the Niño 3.4 region (following Kousky & Higgins, 2007). Also indicated on Figure 12 are the defined El Niño episodes (gray areas above +0.5°C anomalies) and the cold periods (gray areas below −0.5°C anomalies) referred to as La Niña episodes (also after Kousky & Higgins, 2007)]. Although no

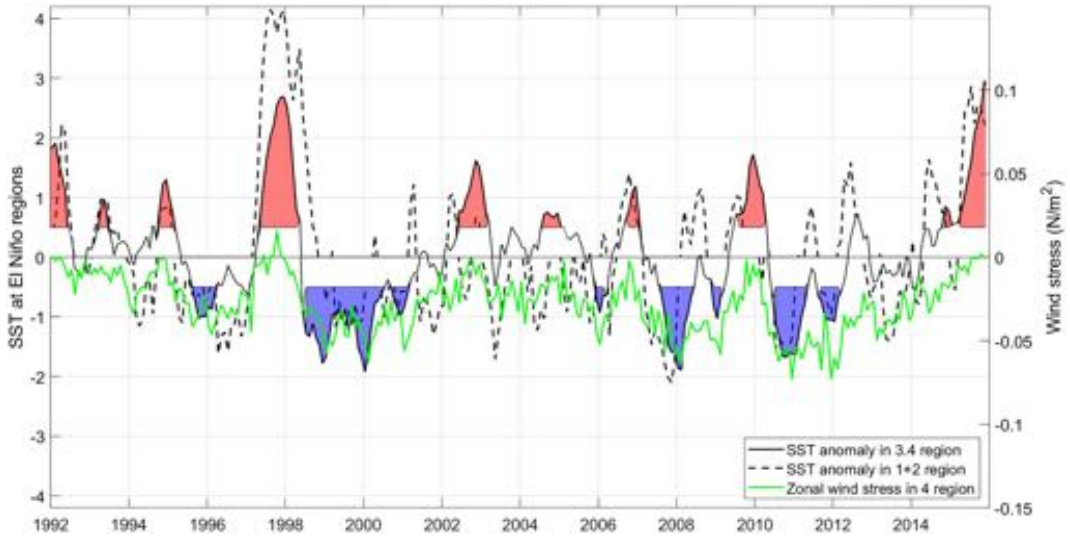

Figure 12. Time series of El Niño Southern Oscillation (ENSO) 1+2 and 3.4 regions from ERSST.v4 SST anomalies in the Niño 3.4 region (5°N–5°S, 120°–170°W) and Niño 1+2 (0–10°S, 90–80°W) (Huang et al., 2015). Also shown is the ERA-1 zonal wind stress from Niño 4 (green line). Geographical locations of the four Niño regions: Niño-1+2 (0–10°S, 90–80°W), Niño 3 (5°N–5°S, 150–90°W), Niño 4 (5°N–5°S, 160°E–150°W), and Niño −3.4 (5°N–5°S, 170–120°W). (Rasmusson & Carpenter, 1982).

more common than El Niño or La Niña periods, unmarked (no shading) periods are considered "normal" conditions.

We have indicated in Figures 4, 6, 8, and 10 the corresponding El Niño (black squares in the top of the plot) and La Niña periods (gray squares in the top of the plot). In general, all coastal stations and TAO buoys show higher heat content and a deepening of the 20°C isotherm, while during "normal" and La Niña periods, the 20°C isotherm is found closer to the surface, and heat content in the upper water column (above 100 m) at

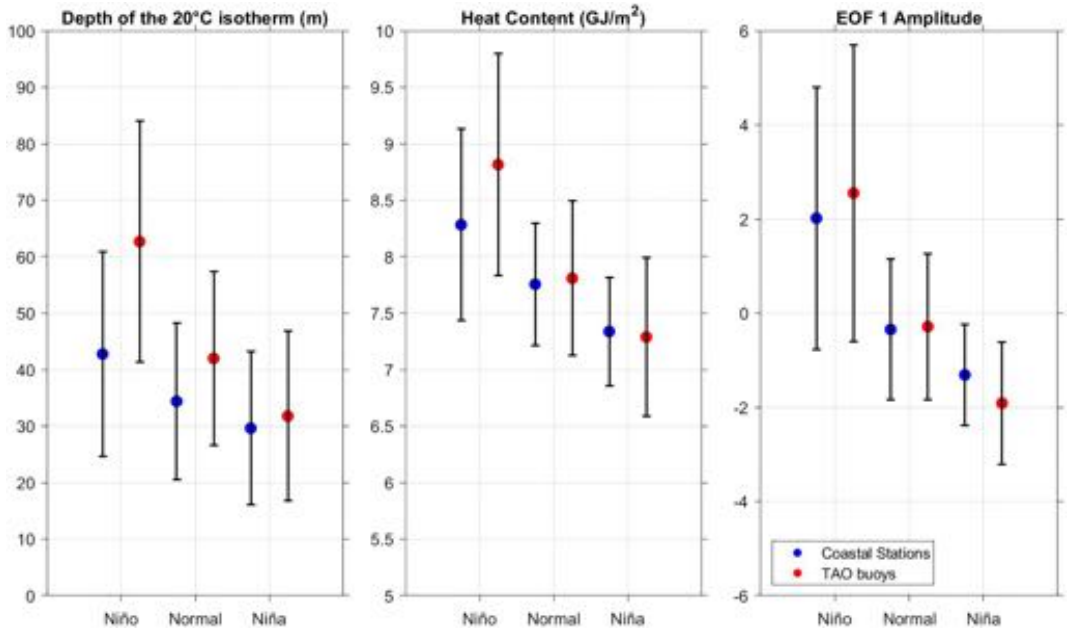

Figure 13. (Left panel) Depth of the 20°C isotherm, (center) heat content, and (right) EOF 1 amplitude from the coastal stations (blue) and TAO buoys (red) separated by Niño (warm), normal and Niña (cold) events. The error bars indicate one standard deviation.

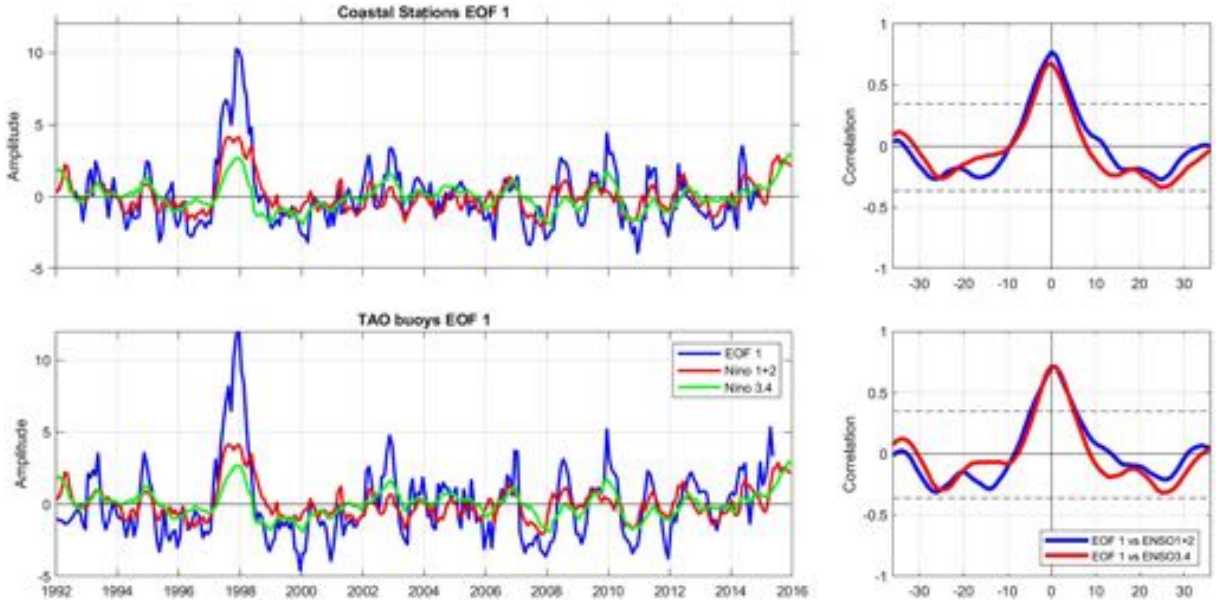

Figure 14. (Left panels) Comparison of empirical orthogonal function (EOF) amplitude time series (blue lines) from analysis of anomaly coastal station data (top) and TAO buoys (bottom) with ENSO 1+2 (red) and ENSO 3.4 (green) indices. (Right panels) Lagged cross correlations between coastal station (top) and TAO buoys (bottom) amplitude EOF time series with ENSO 1+2 (blue) and 3.4 (red) indices. 95% significance levels are shown as dashed lines determined by methods described in Ebisuzaki (1997).

the coastal stations is less than that observed at the TAO buoys to the west of the Gálapagos Islands. Figure 13 shows the mean and standard deviation of the HC, depth of the 20°C isotherm, and the first mode amplitude time series, $A_1(t)$, all from both coastal station and TAO data for El Niño, normal, and La Niña periods. These mean statistics show that the water is warmer during El Niño periods (higher HC, deeper 20°C isotherm, and increased $A_1(t)$), and coldest during La Niña (lower HC, shallower 20°C isotherm, and decreased $A_1(t)$) both at the coastal stations and the TAO buoys. These results are perhaps not unexpected due to established links between ENSO events and coastal upwelling along the coast of Perú (Alheit & Niquen, 2004; Chavez et al., 2008) and Galápagos (Eden & Timmermann, 2004; Karnauskas et al., 2007). Observations at the TAO buoys show deeper thermocline depths, and slightly higher upper water column temperatures and heat content than the coastal data during all periods.

Figure 14 shows a comparison between the first EOF amplitude time series, $A_1(t)$, from the coastal station temperature anomaly data (at 81°W; Table 1) and ENSO 3.4 and 1+2 indices. Qualitatively the records follow a similar oscillation, with larger ENSO values corresponding to El Niño events, particularly during the 1997–1998 event. Also, shown in Figure 14 are lagged cross correlations between $A_1(t)$ and each ENSO index, with $A_1(t)$ significantly correlated to the ENSO index in the central Pacific (Niño 3.4; $R = 0.65$) and eastern equatorial Pacific (Niño 1+2; $R = 0.74$) regions. Significance levels were again determined from the bootstrap method of Ebisuzaki (1997) and summarized in Table 3. Comparisons between $A_1(t)$ of the temperature anomalies observed at the TAO buoys (along 95°W longitude) and 3.4 and 1+2 ENSO indices (also shown in Figure 14) show similar relationships, with significant correlation with the central Pacific (Niño 3.4; $R = 0.71$) and eastern equatorial Pacific (Niño 1+2; $R = 0.86$) that is slightly higher than at the coastal stations.

Table 3
Maximum Cross Correlation Between the EOF Mode 1 Amplitude Time Series From the Coastal Stations (CS) and TAO Buoys With ENSO SST 3.4 and 1+2 Region Indices

		El Niño 3.4	El Niño 1+2
EOF		*R* max	*R* max
Mode 1	CS	0.65 (0.32)	0.74 (0.32)
	TAO	0.71 (0.28)	0.86 (0.28)

Note. 95% significance levels are given in parenthesis determined by Ebisuzaki (1997).

EOF mode 1 variability, $A_1(t)$, for anomaly time series temperature data from both coastal stations and TAO buoys are strongly coupled to each other, and to interannual ENSO variations. Approaches for further analysis of amplitude time series, $A_j(t)$, from EOF decomposition of various ocean temperature data has been suggested by several studies, including subtracting the signal defined by the first EOF, $X_1(x_m, t) = A_1(t)F_1(x_m)$, from the data, $X(x_m, t)$, and then recomputing EOFs on the residual

(as suggested by Enfield & Mestas-Nuñez, 2000; Cane et al., 1997)]. Another method useful for discerning propagating signals (or modes) in the time series array (Rasmusson et al., 1981; Wallace & Dickinson, 1972) involves computing the Hilbert transform, $H()$, of the data such that $Y(x_m, t) = H(X(x_m, t))$, and constructing a complex time series where $Z(x_m, t) = X(x_m, t)+iY(x_m, t)$ that is subjected to a complex EOF analysis (following Enfield & Mestas-Nuñez, 2000). Each of these methods were explored with corresponding amplitude time series of spatial modes compared with ENSO indices; however, no easily deduced insight was obtained. The ENSO signal was present, but is no more illuminating in terms of describing the variability than the present analysis, and in some cases (e.g., the complex decomposition), the interpretation was more difficult.

4.2. Winds

Winds in the far eastern Pacific are strongly influenced by the topography, as well as the location of the South Pacific High, which can influence the southeasterly trade winds and the equatorward (upwelling-favorable) winds along the Pacific coast of South America (Montecinos & Aceituno, 2003; Schneider et al., 2017). Furthermore, the movement of the ITCZ that modulates the teleconnection with the northern Tropical Atlantic (Enfield & Mayer, 1997) creates jets blowing through three gaps in the Central American cordillera, which bound the zonal (SEC, NECC, and NEC) currents of the central Pacific (Alory et al., 2012; Fiedler et al., 1991; Kessler, 2006; Lavín et al., 2006). During El Niño events, the easterly winds in the central Pacific are weakened, giving place to westerly wind bursts, which allow the propagation of warmer waters from the western Pacific to the central Pacific and beyond (Ando & McPhaden, 1997; Menkes et al., 2014; Wyrtki, 1975).

The strong coupling between ENSO indices and the observed temperature structure at the TAO and coastal stations (Figure 14) suggests that the effects of remote El Niño forcing are strongly influencing the Ecuadorian Sea eastward of the Galápagos Islands. However, it is not known how the interannual variations in regional wind fields (possibly coupled with remote wind sources) are related to the temperature structure in the Ecuadorian Sea. In order to examine the relationship between regional wind velocity and the interannual variability of sea temperature at the coastal stations, temperature profile observations are compared with daily averaged zonal and meridional winds (U and V components, respectively, in the usual oceanographic convention) with 0.75° horizontal resolution derived from modeling and observations by the ECMWF Global ERA-Interim reanalysis (Berrisford et al., 2009). This reanalysis is based on a global atmospheric reanalysis from 1979, continuously updated in real time (Dee et al., 2011).

To compare interannual variations in regional ECWMF winds with coastal station data, climatological wind variations were computed and subtracted from the wind time series to produce anomaly wind fields similar to the analysis of the coastal station and TAO buoy temperature profile analysis. To best compare the variability of the regional wind anomalies with the monthly sampled coastal data, the time series were averaged backwards in time 29 days (about 1 month less 1 day) prior to the actual date when the CTD casts were made. This averaging window was applied to every previous time step in the daily wind time series. The temporally averaged zonal and meridional wind time series, $U(v_n, t, \tau)$ and $V(v_n, t, \tau)$, respectively, at the n spatial grid locations, v_n, spanning the eastern equatorial Pacific between 10° north and south of the equator and from 96°W and the coastline, are compared with the first mode EOF amplitude time series, $A_1(t)$, from the long record coastal station data by computing lagged cross-correlations for values of $\tau = 1 - 29$ days. Correlations generally increased as lag, τ, increased, with maximum values occurring at the 29-day averaging time scale.

Figure 15 shows the spatial variation in the maximum correlation (for $\tau = 29$ days, approximately 1 month) between $A_1(t)$ and both $U(v_n, t, \tau)$ and $V(v_n, t, \tau)$. Lags at which the maximum correlation was significant (greater than 0.27 based on analysis methods in Ebisuzaki, 1997) was between 0 and 5 days, indistinguishable from the monthly sampled coastal profile sampling interval. Because the coastal station data are at monthly intervals, higher frequency variability that could be important to ENSO oscillations are not fully resolved. The spatial pattern of the wind correlations to the coastal station data show strong negative correlation ($R = -0.66$) in the Colombian Basin to the north of the coastal stations in both the zonal and meridional winds, suggesting that south-west winds are correlated to warmer waters (positive temperature anomalies) in the coastal stations.

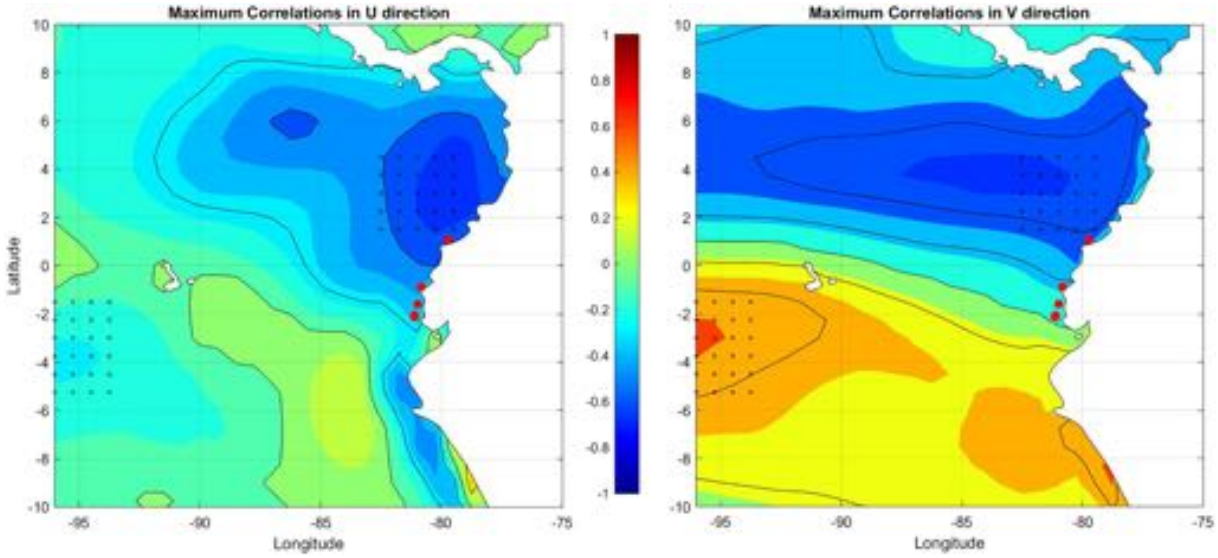

Figure 15. Color contours of cross-correlation between the coastal stations' first empirical orthogonal function mode and monthly averaged (left panel) U and (right panel) V winds obtained from ERA-Interim Reanalysis. Correlation scale is given by the colorbar. The black squares denote areas with largest (positive or negative) correlation and taken for empirical orthogonal function analysis.

Similarly, strong correlations were observed to the north and just offshore the Perú coastline, but with negative correlation to $U(\mathrm{v}_n, t, \tau)$ ($R = -0.5$) and positive correlation to $V(\mathrm{v}_n, t, \tau)$ ($R = 0.5$). In each of these areas, the nature of the correlations suggests that stronger than normal equatorward winds (blowing toward the SW in the Colombian Basin, and toward the NW off the coast of Perú) results in warmer coastal surface waters (i.e., higher values of $A_1(t)$). These winds are favorable for upwelling at latitudes a few degrees north and south of the equator, but not right at the equator where Coriolis goes to zero. Despite upwelling favorable winds to the north and south of the equator, the coastal station temperature anomalies show warmer surface waters, consistent with a convergence of surface wind driven currents and a pilling-up at the equator of warmer Colombian and Peruvian surface waters near the coast. Oppositely, colder waters at the coastal stations, associated with La Niña events are coupled to poleward directed northeastern and southeastern winds (blowing away from the equator) in the Colombian basin and off the coast of Perú (Kessler, 2006). This indicates that wind field variations similar to these close to the coast north and south of the equator are consistent with convergences and divergences of surface waters at the equator, corresponding to warmer surface waters during stronger equatorward winds and colder surface waters during poleward winds.

The correlation between the winds and $A_1(t)$ generally decreased with longitudinal distance away from the coastal station, except for a region to the south west of the Galápagos where meridional winds were significantly correlated ($R = +0.62$), indicating that anomalously northerly winds (equatorward) are coupled to warmer waters in the Ecuadorian Sea. This correlation may arise due to the wind fields themselves being driven by the same larger scale process that is driving the coastal ocean mixed layer dynamics.

To examine the relationship of the observed temperature anomalies with remote winds forcing, we computed cross-correlations of the ERA-1 Niño 4 zonal wind stress fields (shown in Figure 12) with $A_1(t)$ from the TAO and coastal stations (Figure 16). Maximum correlations of 0.54 and 0.51 (95% significant level of 0.25) were observed at the coastal stations and TAO buoys, respectively, with the winds leading at about a 2-month lag. We also computed the cross-correlations with zonal wind stress from the Niño 3.4, Niño 3, and Niño 1+2 regions (Figure 16). The correlations drop off with proximity to the eastern Pacific, with correlations insignificant for the Niño 3 and Niño 1+2 zonal wind stress. The results indicate that the bulk variability of the sea temperature at the coastal stations and most eastern TAO buoy locations are coupled to the remote zonal wind forcing driving the El Niño events. This analysis suggests that interannual wind variations in the central equatorial Pacific (coupled to ENSO variations) are driving the variability in the coastal Ecuadorian sea. The regional wind fields (and the precipitation) are likely responding to the

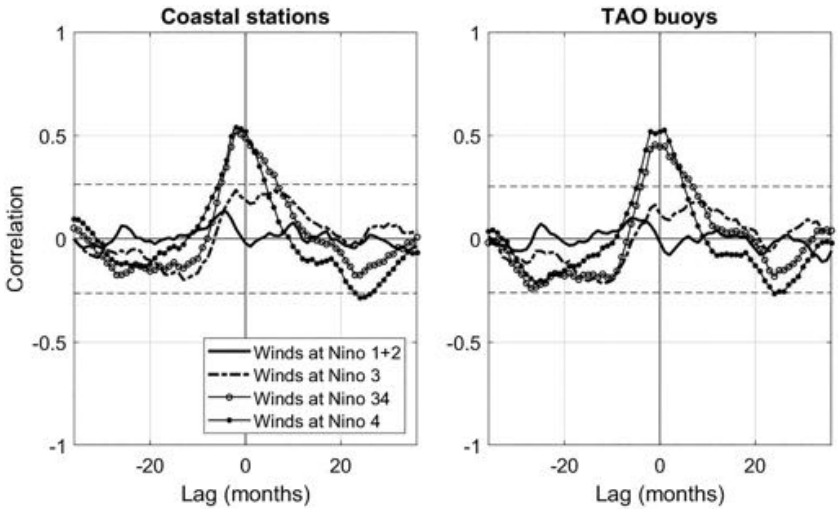

Figure 16. Lagged cross-correlations between coastal stations (left panel) and TAO buoys (right panel) with ERA-1 zonal wind stress from Niño 4 (solid dotted line), Niño 3,4 (open dotted line), Niño 3 (dashed line), and Niño 1+2 (solid line) regions (Figure 12). 95% significance levels are shown as dashed lines determined by methods described in Ebisuzaki (1997).

larger scale processes that drive the SST variability (Morán-Tejeda et al., 2016; Vecchi, 2006; Zhang & McPhaden, 2006).

It is well known that atmospheric variability in the tropics (such as westerly wind bursts and the Madden-Julian Oscillation) contributes to intraseasonal variability and can energize ENSO processes (e.g., McPhaden, 1999; McPhaden, 2004). Because the coastal stations are sampled at monthly intervals, this source of variability is not resolved and manifests as noise in the time series. Further research is needed to understand the impact of extratropical intraseasonal variability on the interannual variability of the Ecuadorian Sea. Nonetheless, the coastal station records show strong interannual variability coupled to ENSO indices and remote zonal wind forcing, most likely due to Eastern Pacific El Niños that have stronger near surface temperature signals much stronger than Central Pacific El Niños (Capotondi et al., 2015; McPhaden et al., 2011).

4.3. Sources of Uncertainty

Observations obtained at the coastal stations occurred on an approximately monthly interval over the course of the data set, with a few periods where no data were collected, the instruments malfunctioned, or the data were deemed unusable. These time series appear qualitatively to well capture the seasonal (climatological) variability; that is, well known seasonal variations in temperature in the upper water column are clearly present. However, the sampling interval is too large to resolve high frequency daily or weekly time scales which can be large owing to intraseasonal variability (Capotondi et al., 2015; McPhaden et al., 2011), presenting the possibility for aliasing in the time series. At the TAO buoys, the data are sampled continuously from fixed sensors at particular depths, and monthly time series determined from averaging. Thus, for TAO data the high frequency variability is averaged out and the possibility of aliasing is generally eliminated from the TAO time series. The climatological data from both the coastal stations and TAO buoys are subtracted from the time series profile and a subsequent EOF decomposition of the anomaly data is performed. Considering that the first EOF mode amplitude time series from the coastal stations is so strongly coupled to the TAO buoy first mode EOF amplitude time series suggests that the interannual variability of the temperature profiles at coastal stations is well captured, and that aliasing is not likely a major problem.

The lag of maximum correlation between the TAO buoys and the coastal station's first EOF mode amplitude time series occurs at zero, indicating a synchronous (at monthly time scales) oscillation of the bulk of the thermal variability associated with ENSO signals. Kessler et al. (1995) suggest that Kelvin waves are observed to be forced west of the date line and propagated eastward at a speed of 2.4 m/s, travelling at approximately

1.9° per day (longitudinally). At this speed the lags at monthly sampling are indistinguishable over the distance between the outer (TAO buoy, 95°W) and inner (Coastal Station, 81.5°W) parts of the study area.

Wind observations were obtained at stations rather close to the coast and may be influenced by local topography and coastal atmospheric gradients induced by local diurnal heating and cooling. Analysis between zonal and meridional wind time series and anomalies in HC, 20°C isotherm depth, and SST time series did not reveal any strong correlation, a result that would be clearly influenced by local effects. The EOF decomposition of the data somewhat isolates the dominant (El Niño) signals from the higher frequency fluctuations. In any case, it is interesting to note the relatively weak effect the local winds have on the upwelling in the region compared to the longer term variability.

As an aside, along with the CTD casts performed monthly at the coastal stations, water samples for chemical properties were taken as reported by Carrillo (2012, 2013). Carrillo suggests that strong El Niño (warm) events produce more oxygenated water columns (see Figure 2 in Carrillo, 2013), while relatively colder periods (La Niña events) before (e.g., 1995/1996) and after (e.g., 1999/2000) warm events produce minimum observed oxygen concentrations throughout the water column. Large changes in oxygen could have potential consequences on the marine ecosystem in general. As indicated in FAO records, a decrease in fisheries capture is recorded during 1982/1983, 1990 and 1997/1998, coincident with warmer periods in the equatorial Pacific. Further analysis linking the effects of seasonal and interannual temperature, salinity and wind variability, would be needed to better understand the ecosystem dynamics and effects on productivity in the Ecuadorian Sea.

5. Conclusions

Monthly time series of temperature and salinity profiles obtained over 22 years at five latitudinally-separated stations located 8 NM from the coast in the Ecuadorian Sea were analyzed and compared to data outside of the Galápagos to examine interannual variability in the upper water column of coastal waters. CTD data were obtained at two of the five stations from 1992 to 2014 by the Oceanographic Institute of the Navy (INOCAR), and at the three other stations from 2004 to 2014 by the National Fisheries Institute (INP) of Ecuador, and are ongoing today. Coastal station data show strong seasonal variability, which is removed by subtracting monthly climatological means from the time series data. These anomaly time series have substantial interannual variability in the 20°C isotherm depth and heat content over the upper 100 m of the water column. Each anomaly time series suffers from data gaps owing to periods when the 20°C isotherm or the mixed-layer depth was below 100 m, nor does it include heat content contributions deeper than 100 m. As a consequence, the time series are more difficult to evaluate. To better represent the anomaly time series data, all profiles are decomposed into orthogonal components using standard EOF analysis (Barnett, 1984).

Two analyses were done on the coastal stations, the first included only the two longest records (spanning 22 years), the second involved all five coastal records, but only spanned the overlapping portions dating back to 2004 (and spanning 11 years). Similar characteristics in the spatial factors were qualitatively observed in the first three EOF modes of each decomposition. Cross-correlations between mode 1 EOF amplitude time series from the short and long record decompositions was very high ($R = 0.95$). The first mode EOF contains the bulk of the variability (70.9%) in the thermocline depth. The second and third spatial modes qualitatively describe variations about the equator (latitudinal changes; 9.92%), and vertical and horizontal variations (8.09%); however, limitations based on possibilities of aliasing in the raw time series and sampling errors make physical interpretation of higher modes not possible.

Comparisons of coastal anomaly time series data are made with observations obtained from TAO/Triton buoys located at 95°W between 2°N and 2°S, just (850 nm) to the west of the Galápagos Islands. Anomaly time series were obtained from the TAO data in a similar manner as for the coastal station data, and subsequently subjected to the same EOF decomposition. The first three spatial EOF modes at the TAO stations (representing 71.1, 7.35, and 6.06% of the variance) describe variability in the thermocline depth, and latitudinal variations, qualitatively similar to observations from the coastal stations. Cross-correlations show that the first mode EOF amplitude time series from the TAO buoys and coastal stations is very strongly correlated ($R = 0.86$), showing that the bulk of the temperature profile interannual variability close to shore (within 8 NM) is strongly coupled to variability to the west of the Galápagos Islands outside of the topographically

delineated Ecuadorian Sea. Higher mode EOFs cannot be distinguished from sampling errors (following analysis of North et al., 1982).

The first mode EOF amplitude time series at the coastal stations and TAO buoys were also compared with ENSO indices derived from satellite SST observations. Results show that first mode EOFs from both the coastal stations and TAO buoys were significantly correlated to the ENSO signal of SST anomaly at regions 3.4 and 1+2.

The first EOF mode of the coastal stations was compared to regional wind data averaged over the previous 29 days from ECMWF ERA-Interim Global reanalysis. Highest correlations were found close to the coast, north and south of the coastal stations, in the Colombian Basin, off the coast of Perú to the south, and southwest of the Galápagos. Cross-correlation of the remote zonal wind stress from the Niño 4 region in the central Pacific was found to be coupled to the sea temperature variability at the coastal stations and the most eastern TAO buoys, with correlations to first mode EOF amplitude time series of 0.54 and 0.51, respectively. The strong coupling between ENSO indices and remote wind forcing with the observed temperature structure at the coastal stations off the Ecuador coast suggests that the effects of El Niño forcing are strongly influencing the Ecuadorian Sea eastward of the Galápagos.

Future work needs to focus on extending the spatial variability of the study area from the coast towards the Galápagos Islands, for which several sources of data have been identified and developed in the Eastern-Pacific countries from international agreements, such as the South Pacific Permanent Commission (CPPS). Seasonal cruises, once a year in the Ecuadorian Sea (as well as north and south of the country, coordinated by the CPPS) since the early 1980s would provide better spatial information of the water column down to 500 m of depth from the South American coast to west of the Galápagos Islands. Better understanding of the influence of the Colombia Basin and Humboldt current on interannual variability of the Ecuadorian Coastal stations could be achieved by including buoy data from Perú's National Hydrography Direction of the Navy (DHN), as well as coastal stations from the Colombian Oceanographic and Hydrographic Research center of the Pacific (CPPS - Dimar).

Acknowledgments
Support for M. J. Marín Jarrín was provided by a Scholarship from the Secretary of Higher Education, Science, Technology and Innovation of the Republic of Ecuador. Additional funding was provided by the University of New Hampshire Graduate School, School of Marine Science and Ocean Engineering, and the Oceanography Graduate Program. The two long coastal stations data sets (La Libertad and Manta) have been obtained from the Dept. of Ocean Sciences at the National Oceanographic Institute of the Navy of Ecuador (INOCAR). Special thanks to each and every individual who surveyed the stations, cooperated in the logistics of those or have looked into the time series. The three shorter records from Esmeraldas, Puerto López and Salinas have been obtained from different programs in the National Fisheries Institute (INP) and National Institute of Meteorology and Hydrology (INAMHI) of Ecuador. Special thanks to the oceanographers, as well as the fishermen who cooperated in obtaining data from these important areas. Data can be obtained directly by contacting INOCAR, INP, and INAMHI. TAO buoy data can be obtained from GTMBA Project Office of NOAA/PMEL (https://www.pmel.noaa.gov/tao/drupal/disdel). Daily-OI-V2 final data (AVHRR) version 2.0 can be obtained from NOAA/OAR/ESRL PSD Boulder, CO (https://www.esrl.noaa.gov/psd/). Global wind data are from ECMWF (https://apps.ecmwf.int/datasets/data/intermin-full-daily/levtype-sfc/). We thank the anonymous reviewers whose comments greatly improved the paper.

References

Alheit, J., & Niquen, M. (2004). Regime shifts in the Humboldt Current ecosystem. *Progress in Oceanography*, *60*(2–4), 201–222. https://doi.org/10.1016/j.pocean.2004.02.006

Alory, G., Maes, C., Delcroix, T., Reul, N., & Illig, S. (2012). Seasonal dynamics of sea surface salinity off Panama: The far eastern Pacific Fresh Pool. *Journal of Geophysical Research*, *117*(4), 1–13. https://doi.org/10.1029/2011JC007802

Ando, K., & McPhaden, M. J. (1997). Variability of surface layer hydrography in the tropical Pacific Ocean. *Journal of Geophysical Research*, *102*(C10), 23,063–23,078. https://doi.org/10.1029/97JC01443

Ballón, M., Wosnitza-Mendo, C., Guevara-Carrasco, R., & Bertrand, A. (2008). The impact of overfishing and El Niño on the condition factor and reproductive success of Peruvian hake, Merluccius gayi peruanus. *Progress in Oceanography*, *79*(2–4), 300–307. https://doi.org/10.1016/j.pocean.2008.10.016

Barnett, T. P. (1984). Interaction of the Monsoon and Pacific Trade Wind System at Interannual Time Scales. Part III: A Partial Anatomy of the Southern Oscillation. *Monthly Weather Review*, *112*(12), 2388–2400. https://doi.org/10.1175/1520-0493(1984)112<2388:IOTMAP>2.0.CO;2

Berrisford, P., Dee, D., Fielding, K., Fuentes, M., Kallberg, P., Kobayashi, S., & Uppala, S. (2009). The ERA-Interim Archive. *ERA Rep. Ser.*, *1*(1), 1–16.

Bertrand, S., Dewitte, B., Tam, J., Díaz, E., & Bertrand, A. (2008). Impacts of Kelvin wave forcing in the Peru Humboldt Current system: Scenarios of spatial reorganizations from physics to fishers. *Progress in Oceanography*, *79*(2–4), 278–289. https://doi.org/10.1016/j.pocean.2008.10.017

Cane, M., Clement, A., Kaplan, A., Kushnir, Y., Pozdnyakov, D., Seager, R., et al. (1997). Twentieth-Century Sea Surface Temperature Trends. *Science*, *275*(5302), 957–960. https://doi.org/10.1126/science.275.5302.957

Capotondi, A., Wittenberg, A. T., Newman, M., Di Lorenzo, E., Yu, J.-Y., Braconnot, P., et al. (2015). Understanding ENSO Diversity. *Bulletin of the American Mathematical Society*, *96*(6), 921–938. https://doi.org/10.1175/bams-d-13-00117.1

Carrillo, P. (2012). Comportamiento Del Oxigeno Disuelto En Dos Estaciones Costeras La Libertad Y Manta, Como Aporte Al Conocimiento Del Fenómeno "El Niño,". *Acta Oceanográfica Del Pacífico*, *17*.https://www.oceandocs.org/bitstream/handle/1834/4655/Comportamiento del oxigeno disuelto en dos estaciones.....pdf?sequence=1

Carrillo, P. (2013). Comportamiento del oxígeno disuelto en la columna de agua de las estaciones fijas ecuatorianas 1988-2013. *Acta Oceanográfica Del Pacífico*, *18*(1), 41–48. https://www.inocar.mil.ec/web/phocadownloadpap/actas_oceanograficas/acta18/OCE1801_4.pdf

Chavez, F. P., Bertrand, A., Guevara-Carrasco, R., Soler, P., & Csirke, J. (2008). The northern Humboldt Current System: Brief history, present status and a view towards the future. *Progress in Oceanography*, *79*(2–4), 95–105. https://doi.org/10.1016/j.pocean.2008.10.012

Chavez, F. P., Strutton, P. G., Friederich, G. E., Feely, R. A., Feldman, G. C., Foley, D. G., & McPhaden, M. J. (1999). Biological and chemical response of the equatorial pacific ocean to the 1997-98 El Niño. *Science (80-.)*, *286*(5447), 2126–2131. https://doi.org/10.1126/science.286.5447.2126

Chelton, D. B. (1983). Effects of sampling errors in statistical estimation. *Deep Sea Research*, *30*(10A), 1083–1103. https://doi.org/10.1016/0198-0149(83)90062-6

Cornejo-Rodríguez, M. d. P. (1987). Ondas Ecuatoriales atrapadas: Ondas mezcladas de Rossby - gravedad. *Acta Ocean. del Pacifico*, *4*(1), 204–210. https://www.inocar.mil.ec/web/index.php/publicaciones/actas-oceanograficas/file/56-ondas-ecuatoriales-atrapadas-ondas-mezcladas-de-rossby-gravedad?start=10

Cornejo-Rodríguez, M. d. P., & Enfield, D. B. (1987). Propagation and Forcing of High-Frequency Sea Level Variability Along the West Coast of South America. *Journal of Geophysical Research*, *92*(C13), 14323–14334. https://doi.org/10.1029/jc092ic13p14323

de Boyer Montégut, C., Madec, G., Fischer, A. S., Lazar, A., & Iudicone, D. (2004). Mixed layer depth over the global ocean: An examination of profile data and a profile-based climatology. *Journal of Geophysical Research, C Oceans*, *109*(12), 1–20. https://doi.org/10.1029/2004JC002378

Dee, D. P., Uppala, S. M., Simmons, A. J., Berrisford, P., Poli, P., Kobayashi, S., et al. (2011). The ERA-Interim reanalysis: Configuration and performance of the data assimilation system. *Quarterly Journal of the Royal Meteorological Society*, *137*(656), 553–597. https://doi.org/10.1002/qj.828

Deng, W., Wei, G., Xie, L., Ke, T., Wang, Z., Zeng, T., & Liu, Y. (2013). Variations in the Pacific Decadal Oscillation since 1853 in a coral record from the northern South China Sea. *Journal of Geophysical Research: Oceans*, *118*, 2358–2366. https://doi.org/10.1002/jgrc.20180

Dijkstra, H. A. (2008). *Dynamical Oceanography*. Berlin Heidelberg, 407pp.: Springer-Verlag. https://doi.org/10.1007/978-3-540-76376-5

Ebisuzaki, W. (1997). A method to estimate the statistical significance of a correlation when the data are serially correlated. *Journal of Climate*, *10*(9), 2147–2153. https://doi.org/10.1175/1520-0442(1997)010<2147:AMTETS>2.0.CO;2

Eden, C., & Timmermann, A. (2004). The influence of the Galápagos Islands on tropical temperatures, currents and the generation of tropical instability waves. *Geophysical Research Letters*, *31*, L15308. https://doi.org/10.1029/2004GL020060

Enfield, D. B., Cornejo-Rodríguez, M. d. P., Smith, R. L., & Newberger, P. A. (1987). The Equatorial Source of propagating variability along the Peru Coast during the 1982-1983 El Niño. *Journal of Geophysical Research*, *92*(C13), 14335–14346. https://doi.org/10.1029/jc092ic13p14335

Enfield, D. B., & Mayer, D. A. (1997). Tropical Atlantic sea surface temperature variability and its relation to El Niño-Southern Oscillation. *Journal of Geophysical Research*, *102*(C1), 929–945. https://doi.org/10.1029/96JC03296

Enfield, D. B., & Mestas-Nuñez, A. M. (2000). Global Modes of ENSO and non-ENSO Sea Surface Temperature Variability and Their Associations with Climate. *El Niño South. Oscil. Multiscale Var. Glob. Reg. Impacts.*, 89–112. https://doi.org/10.1017/cbo9780511573125.004

Fiedler, P. C., Philbrick, V., & Chavez, F. P. (1991). Oceanic upwelling and productivity in the eastern tropical Pacific. *Limnology and Oceanography*, *36*(8), 1834–1850. https://doi.org/10.4319/lo.1991.36.8.1834

Fiedler, P. C., & Talley, L. D. (2006). Hydrography of the eastern tropical Pacific: A review. *Progress in Oceanography*, *69*(2–4), 143–180. https://doi.org/10.1016/j.pocean.2006.03.008

Fofonoff, N. P., & Millard, R. C. Jr. (1983). Algorithms for the computation of fundamental properties of seawater. *UNESCO Tech. Pap. Mar. Sciences*, *44*. 53pp.

Glynn, P. W., Maté, J. L., Baker, A. C., & Calderón, M. O. (2001). Coral Bleaching and Mortality in Panama and Ecuador During the 1997–1998 El Niño–Southern Oscillation Event: Spatial/Temporal Patterns and Comparisons With the 1982–1983 Event. *Bulletin of Marine Science*, *69*(1), 79–109. https://www.ingentaconnect.com/contentone/umrsmas/bullmar/2001/00000069/00000001/art00007

Huang, B., Banzon, V. F., Freeman, E., Lawrimore, J., Liu, W., Peterson, T. C., et al. (2015). Extended reconstructed sea surface temperature version 4 (ERSST.v4). Part I: Upgrades and intercomparisons. *Journal of Climate*, *28*(3), 911–930. https://doi.org/10.1175/JCLI-D-14-00006.1

Huffman, G. J., Bolvin, D. T., Nelkin, E. J., Wolff, D. B., Adler, R. F., Gu, G., et al. (2007). The TRMM Multisatellite Precipitation Analysis (TMPA): Quasi-Global, Multiyear, Combined-Sensor Precipitation Estimates at Fine Scales. *Journal of Hydrometeorology*, *8*(1), 38–55. https://doi.org/10.1175/JHM560.1

Jeronimo, G., & Gomez-Valdes, J. (2010). Mixed layer depth variability in the tropical boundary of the California Current, 1997-2007. *Journal of Geophysical Research, Oceans*, 115(5). https://doi.org/10.1029/2009JC005457

Karnauskas, K. B., Murtugudde, R., & Busalacchi, A. J. (2007). The Effect of the Galápagos Islands on the Equatorial Pacific Cold Tongue. *Journal of Physical Oceanography*, *37*(5), 1266–1281. https://doi.org/10.1175/JPO3048.1

Kessler, W. S. (2006). The circulation of the eastern tropical Pacific: A review. *Progress in Oceanography*, *69*(2–4), 181–217. https://doi.org/10.1016/j.pocean.2006.03.009

Kessler, W. S., McPhaden, M. J., & Weickmann, K. M. (1995). Forcing of intraseasonal Kelvin waves in the equatorial Pacific. *Journal of Geophysical Research*, *100*(C6), 10613. https://doi.org/10.1029/95JC00382

Kousky, V. E., & Higgins, R. W. (2007). An Alert Classification System for Monitoring and Assessing the ENSO Cycle. *Weather and Forecasting*, *22*(2), 353–371. https://doi.org/10.1175/WAF987.1

Lavín, M. F., Fiedler, P. C., Amador, J. A., Ballance, L. T., Färber-Lorda, J., & Mestas-Nuñez, A. M. (2006). A review of eastern tropical Pacific oceanography: Summary. *Progress in Oceanography*, *69*(2–4), 391–398. https://doi.org/10.1016/j.pocean.2006.03.005

Lee, T., Lagerloef, G., Gierach, M. M., Kao, H. Y., Yueh, S., & Dohan, K. (2012). Aquarius reveals salinity structure of tropical instability waves. *Geophysical Research Letters*, *39*, L12610, 1–6. https://doi.org/10.1029/2012GL052232

Levitus, S., Antonov, J. I., Boyer, T. P., Baranova, O. K., Garcia, H. E., Locarnini, R. A., et al. (2012). World ocean heat content and thermosteric sea level change (0-2000m), 1955-2010. *Geophysical Research Letters*, *39*, L10603. https://doi.org/10.1029/2012GL051106

Lucero, M., & Cornejo-Rodríguez, M. d. P. (1990). Evidencia de la Corriente de Cromwell entre 92°W y 84°W, observada en periodos normales y durante El Niño 82-83. *Acta Ocean. del Pacifico*, *6*(1), 17–27. https://www.inocar.mil.ec/web/phocadownloadpap/actas_oceanograficas/acta6/OCE601_3.pdf

McPhaden, M. J. (1999). Genesis and evolution of the 1997-98 El Niño. *Science*, *283*(5404), 950–954. https://doi.org/10.1126/science.283.5404.950

McPhaden, M. J. (2004). Evolution of the 2002/03 El Niño. *Bulletin of the American Mathematical Society*, *85*(5), 677–695. https://doi.org/10.1175/BAMS-85-5-677

McPhaden, M. J. (2012). A 21st century shift in the relationship between ENSO SST and warm water volume anomalies. *Geophysical Research Letters*, *39*, L09706. https://doi.org/10.1029/2012GL051826

McPhaden, M. J., Busalacchi, A. J., Cheney, R., Donguy, J.-R., Gage, K. S., Halpern, D., et al. (1998). The tropical ocean global atmosphere observing system: A decade of progress. *Journal of Geophysical Research*, *103*(C7), 14,169–14,240. https://doi.org/10.1029/97JC02906

McPhaden, M. J., Lee, T., & McClurg, D. (2011). El Niño and its relationship to changing background condition in the tropical Pacific Ocean. *Geophysical Research Letters*, *38*, L15709. https://doi.org/10.1029/2011GL048275

Menkes, C. E., Lengaigne, M., Vialard, J., Puy, M., Marchesiello, P., Cravatte, S., & Cambon, G. (2014). About the role of Westerly Wind Events in the possible development of an El Niño in 2014. *Geophysical Research Letters*, *41*, 6476–6483. https://doi.org/10.1002/2014GL061186

Michaud, F., Proust, J. N., Collot, J. Y., Lebrun, J. F., Witt, C., Ratzov, G., et al. (2015). Quaternary sedimentation and active faulting along the Ecuadorian shelf: preliminary results of the ATACAMES Cruise (2012). *Marine Geophysical Researches*, *36*(1), 81–98. https://doi.org/10.1007/s11001-014-9231-y

Montecinos, A., & Aceituno, P. (2003). Seasonality of the ENSO--related rainfall variability in central Chile and assocaited circulation anomalies. *Journal of Climate*, *16*(2), 281–296. https://doi.org/10.1175/1520-0442(2003)016<0281:SOTERR>2.0.CO;2

Morán-Tejeda, E., Bazo, J., Lopez-Moreno, J. I., Aguilar, E., Azorin-Molina, C., Sanchez-Lornzo, A., et al. (2016). Climate trends and variability in Ecuador (1966-2011). *International Journal of Climatology*, n/a–n/a. https://doi.org/10.1002/joc.4597

North, G. R., Bell, T. L., Cahalan, R. F., & Moeng, F. J. (1982). Sampling errors in the estimation of empirical orthogonal functions. *Monthly Weather Review*, *110*, 699–706. https://doi.org/10.1175/1520-0493(1982)110<0699:SEITEO>2.0.CO;2

Rasmusson, E. M., Arkin, P. A., Chen, W.-Y., & Jalickee, J. B. (1981). Biennial Variations in Surface Temperature over the United States as Revealed by Singular Decomposition. *Monthly Weather Review*, *109*(3), 587–598. https://doi.org/10.1175/1520-0493(1981)109<0587:BVISTO>2.0.CO;2

Rasmusson, E. M., & Carpenter, T. H. (1982). Variations in tropical sea surface temperature and surface wind fields associated with the Southern Oscillation/El Niño. *Monthly Weather Review*, *110*(5), 354–384. https://doi.org/10.1175/1520-0493(1982)110<0354:VITSST>2.0.CO;2

Reynolds, R. W., Smith, T. M., Liu, C., Chelton, D. B., Casey, K. S., & Schlax, M. G. (2007). Daily high-resolution blended analyses for sea surface temperature. *Journal of Climate*, *20*, 5473–5496. https://doi.org/10.1175/2007jcli1824.1

Schneider, W., Donoso, D., Garcés-Vargas, J., & Escribano, R. (2017). Water-column cooling and sea surface salinity increase in the upwelling region off central-south Chile driven by a poleward displacement of the South Pacific High. *Progress in Oceanography*, *151*, 38–48. https://doi.org/10.1016/j.pocean.2016.11.004

Sprintall, J., & Roemmich, D. (1999). Characterizing the structure of the surface layer in the Pacific Ocean. *Journal of Geophysical Research*, *104*(C10), 23,297–23,311. https://doi.org/10.1029/1999jc900179

Thomson, R. E., & Fine, I. V. (2003). Estimating mixed layer depth from oceanic profile data. *Journal of Atmospheric and Oceanic Technology*, *20*(2), 319–329. https://doi.org/10.1175/1520-0426(2003)020<0319:EMLDFO>2.0.CO;2

US Army Corps of Engineers (1998). Water resources assessment of Ecuador, US Army Corps of Engineers, http://www.sam.usace.army.mil/Portals/46/docs/military/engineering/docs/WRA/Ecuador/Ecuador%20WRA%20English.pdf ().

Vargas-Angel, B., Zapata, F. A., Hernandez, H., & Jimenez, J. M. (2001). Coral and coral reef responses to the 1997-98 El Niño event on the Pacific coast of Colombia. *Bulletin of Marine Science*, *69*(1), 111–132.https://www.ingentaconnect.com/content/umrsmas/bullmar/2001/00000069/00000001/art00008

Vecchi, G. A. (2006). The Termination fo the 1997-98 El Nino. Part II: mechanisms of atmospheric change. *Journal of Climate*, *19*, 2647–2664. https://doi.org/10.1175/jcli3780.1

Wade, M., Caniaux, G., & Du Penhoat, Y. (2011). Variability of the mixed layer heat budget in the eastern equatorial Atlantic during 2005-2007 as inferred using Argo floats. *Journal of Geophysical Research, Oceans*, *116*(8), 1–17. https://doi.org/10.1029/2010JC006683

Wallace, J. M., & Dickinson, R. E. (1972). Empirical Orthogonal Representation of Time Series in the Frequency Doman. Part I: Theoretical Considerations. *Journal of Applied Meteorology*, *11*(6), 887–892. https://doi.org/10.1175/1520-0450(1972)011<0887:EOROTS>2.0.CO;2

Wyrtki, K. (1975). El Niño—The Dynamic Response of the Equatorial Pacific Oceanto Atmospheric Forcing. *Journal of Physical Oceanography*, *5*(4), 572–584. https://doi.org/10.1175/1520-0485(1975)005<0572:ENTDRO>2.0.CO;2

Wyrtki, K. (1981). An estimate of equatorial upwelling in the pacific. *Journal of Physical Oceanography*, *11*, 1205–1214. https://doi.org/10.1175/1520-0485(1981)011<1205:aeoeui>2.0.co;2

Zhang, X., & McPhaden, M. J. (2006). Wind stress variations and interannual sea surface temperature anomalies in the eastern equatorial pacific. *Journal of Climate*, *19*, 226–227. https://doi.org/10.1175/jcli3618.1